THESIS

FROM RECYCLED MACHINING WASTE TO USEFUL POWDERS: SUSTAINABLE

FABRICATION AND UTILIZATION OF FEEDSTOCK POWDER FOR METAL ADDITIVE

MANUFACTURING

Submitted by

Blake Patrick Fullenwider

Department of Mechanical Engineering

In partial fulfillment of the requirements

For the Degree of Master of Science

Colorado State University

Fort Collins, Colorado

Summer 2018

Master's Committee:

    Advisor: Kaka Ma

    Chris Weinberger
    James Neilson

ABSTRACT

FROM RECYCLED MACHINING WASTE TO USEFUL POWDERS: SUSTAINABLE

FABRICATION AND UTILIZATION OF FEEDSTOCK POWDER FOR METAL ADDITIVE

MANUFACTURING

Gas atomized (GA) powders are the most common feedstock for state-of-the-art metal additive manufacturing (AM) technologies because of their spherical morphology and controllable particle size distribution. However, significant resource consumption, e.g., energy and inert gas, are required to produce GA powders, leading to high costs and limited availability in alloy compositions. To fulfill the growing demand for alternative and sustainable feedstock production for metal AM, my research aimed to explore a mechanical milling strategy to fabricate 304L stainless steel powders from recycled machining waste chips. A theoretical analysis was performed to evaluate the impact force on powder and the consequent maximum deformation depth per impact during ball milling with different ball diameters. The modeling results suggest that 20-mm-diameter balls effectively reduce the powder particle size while 6-mm-diameter balls are favorable in terms of forming spherical morphology of the powder. Various ball milling procedures were implemented to experimentally investigate the effect of ball diameter on the powder morphology evolution and particle size refinement. It is found that a novel dual-stage ball milling strategy effectively converts machining chips to powder with desirable characteristics (near spherical morphology with particle sizes of 38-150 μm) for metal additive manufacturing.

The ball milled powders created from the machining chips also exhibit a higher hardness than GA powder, based on nanoindentation testing.

To verify the viability of using the ball milled powder created from machining chips in metal AM, single tracks (ST) have been successfully deposited via laser engineered net shaping (LENS®) and compared to the single tracks made from GA powder (ST-GA) using identical deposition conditions. The microstructures of these single tracks exhibited adequate adhesion to the substrate, a uniform melt pool geometry, continuity, and minimal splatter. Minimal differences in grain structure were observed between the single tracks made from ball milled powder (ST-BM) and ST-GA. However, the average nanoindentation hardness of ST-BM is approximately 21% higher than that of ST-GA. Although the chemical compositions of both types of single tracks are within the compositional range of a 304L stainless steel, the increase in hardness of ST-BM is attributed to a 1.7 wt.% decrease in Ni content, potentially leading to an increase in the amount of martensite. Therefore, my research has discovered a sustainable approach to fabricate powders from recycled machining chips and has proved it is feasible to utilize these powders as feedstock in metal AM. Future work on depositing bulk samples with more complex geometry using the ball milled powder is proposed.

ACKNOWLEDGEMENTS

Several other students from The Factory have helped me to compose this research through conversation and technical writing. They include Adam Kuehster, Trevor Aguirre, Alex Preston, Patrick Rodriguez, Mark Bourgeois, Luke Nibbelink, and Daniel Fuqua. For their guidance and support I am thankful.

Finally, I would like to express my gratitude for my wife, daughter, and parents for their loving support throughout my years of study and the process of writing this thesis. Without the encouragement of my family this accomplishment would not be possible.

TABLE OF CONTENTS

LIST OF TABLES

x

Chapter 1　　　Introduction

Metal additive manufacturing (AM) has emerged as a sustainable and competitive processing technology relative to traditional metallurgical manufacturing techniques, such as casting and forging, attributed to the ability of metal AM to create near-net-shapes in a single step. An introduction to the background of the metal AM processes is provided in this chapter, with a focus on discussion of the requirement and characteristics of the feedstock powder. A variety of ball milling techniques are discussed along with a literature review on previous studies that have produced powder with properties near to those used as feedstock in metal AM. In addition, the motivation and the objectives of this work are discussed at the end of this chapter, including the proposition of recycling metal machining chips to produce feedstock powder useable for metal AM by ball milling.

1.1　Metal Additive Manufacturing

1.1.1 AM Technologies

Powder metallurgy (PM) processing techniques, such as AM, thermal spray, spark plasma sintering, and hot isostatic pressing, are widely used to fabricate bulk samples from metal powders. PM processes greatly reduce the need to use metal removal processes and thereby drastically reduce yield losses of manufacturing [1]. The properties of the bulk components created through PM processes depend on both the processing method and the feedstock powder properties [2]. In recent decades, metal AM has attracted increasing research interest because of its capability to create near-net-shape parts, which reduces the need for subsequent machining and the use of hazardous cutting fluids [3]. Thus, metal AM

1

is regarded as a more sustainable process when compared to conventional processing such as casting [3–5]. Images of processing and parts created by laser engineered net shape (LENS®), a metal AM technique, are shown in Figure 1.1.
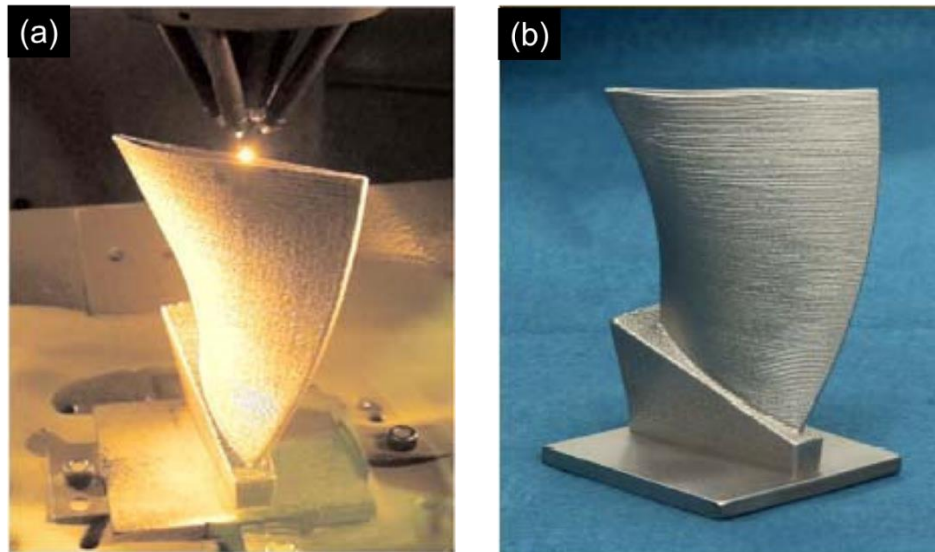
Figure 1.1: (a) LENS® processing of blade and (b) final built blade (courtesy of Optomec Inc.)

Metal AM processing techniques can be categorized into powder bed and powder feed systems (Figure 1.2) [6]. In AM powder bed systems, such as direct metal laser sintering (DMLS), selective laser melting (SLM), selective laser sintering (SLS), and electron beam melting (EBM), a powder bed is created by raking powder across the work area. The powder on the surface layer of the bed is melted or sintered by the energy source (electron beam or laser beam) to form the desired shape via programming aided control. Additional powder is raked across the work area, and the process is repeated to create a solid three-dimensional component. In AM powder feed systems, such as laser engineered net shape LENS® deposition, the powder is fed through nozzles by the carrier gas, typically Ar, onto the build surface. A laser is used to melt a monolayer or more of the powder to build bulk components with a designed shape. A three-dimensional component is created layer by layer by repeating

the process. Powder bed systems possess advantages of producing high resolution features, internal passages, and maintaining dimensional control, while powder feed systems are advantageous because of their larger build volume and their capability to refurbish worn or damaged components [6]. Both systems commonly use gas-atomized (GA) powder as feedstock.
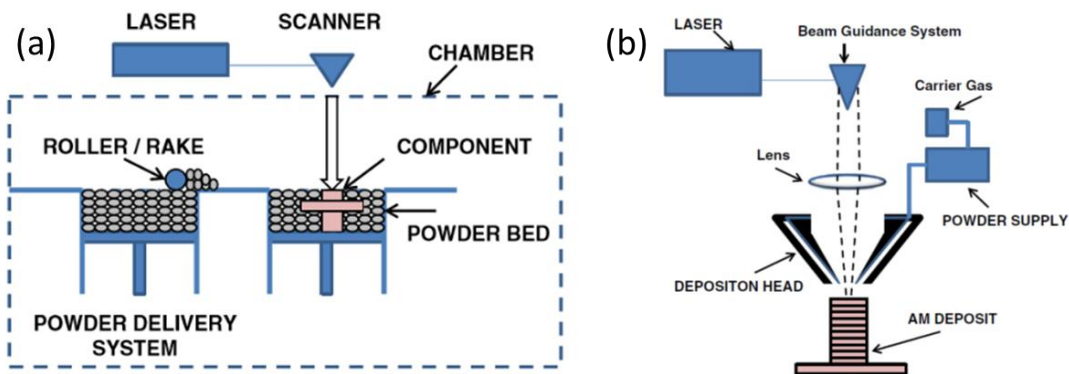
Figure 1.2: Generic illustration of (a) powder bed and (b) powder feed systems [6]

While metal AM is claimed to be sustainable since it is supposed to use only the amount of the powder necessary for the final part, this is not the case. Due to present inefficiencies of metal AM, more than 70% of the feedstock powder will not be fused to the part [7]. This excess powder is often regarded as waste, and is not reused for subseuent deposition [3]. This practice is envornmentally and economically expensive which reduces the sustainbility of metal AM. The present inefficiencies in metal AM could be improved by redesign of metal AM equipment for more efficient usage of powder or creation and utilization of more sustainable powder.

1.1.2 Feedstock for Metal AM

Virgin GA powder is the most common feedstock for AM attributed to its spherical morphology and controllable particle size distribution. However, production of GA powders

requires the metal to reach temperatures beyond their melting point while limiting oxide formation. As such, GA powder production consumes large amounts of energy, inert gas, and produces significant CO_2 emissions (when burning natural gas or coal to melt the metal) [8]. In addition to inefficiencies in powder production, unfused powder is often not reused and becomes waste [7]. To increase sustainability in metal AM it is in demand to explore both the reuse of unfused powder and alternative powder production methods. The flowability of powder in metal AM equipment and the retention of chemical composition in the final part are key to metal AM part manufacture [2,9–14]. Therefore, the primary criteria to produce feedstock powder for metal AM include acceptable morphology, chemical composition, and controllable particle size distribution [10,15,16].

A simplified definition of powder flowability is the ability of a powder to flow through a device or equipment. The flowability generally refers to a qualitative observation of the mass flow of powder through a device or simple a funnel. Powder flowability depends on the physical properties of a material, environmental conditions, and the equipment used for handling [17]. No single test is used to directly quantify the flowability of a powder in all equipment. Several gravity assisted testing methods such as Hall and Carney funnel testing, angle of repose, and avalanche angle is used to compare powder flow and packing against a standard that is known to have high flowability [2,8,18,19]. Other methods such as shear cell testing is used to determine powder-powder friction and powder-wall friction [20–23]. However, powders with a spherical morphology have been found to have higher flowability and bulk density than powders with irregular morphology [19,24,25]. In metal AM, powders with a high flowability move through equipment efficiently, and powders with high bulk density increase the efficiency and resolution of powder bed systems [2,8,19].

The effect of recycling GA powder is often evaluated on a cyclical basis where the properties of recycled powder are examined before subsequent reuse. After sieving and removing particles with sizes above 80 μm, recycled GA stainless steel (SS) powder and CoCr powder contained a higher weight percentage of powder particles below 30 μm when compared to virgin GA powders and the powder from previous recycling cycles [26]. In contrast, recycled GA Ti-6Al-4V powder exhibited fewer particles below 40 μm with increasing numbers of cycles, along with increased oxygen content, decreased sphericity, fewer satellite particles, increased flowability, and consistent alloy compositions [27]. The decrease in sphericity observed in these recycled powders had a less negative effect on the flowability of the powder than the decreased number of satellite particles. Satellite particles often form during the atomization process as particles collide while cooling. Recycled GA IN718 powder subjected to intermediate drying and sieving steps had similar particle size distributions after 14 iterations, with no obvious changes in oxygen content [28]. The unchanged material composition of this study was particularly interesting as the oxygen content of the fabrication chamber is approximately 2000 ppm, significantly higher than other metal AM equipment. The variance of properties of the powder after several recycling times across multiple studies suggests that a standardized testing and characterization approach is in demand to identify the efficiency of using recycled GA powder in metal AM.

Water atomized (WA) powders have also been used as feedstock for metal AM when faster powder solidification rates and a reduction in production cost are desired [2,11]. Compared to GA powders, WA powders often exhibit smaller particle sizes, a wider particle size distribution and relatively irregular shape (Figure 1.3). However, the oxide formation in the materials processed though WA is more difficult to control when compared to GA [2].

5

Despite the stark differences in morphology and particle size distribution, minimal differences have been reported in terms of powder flowability, laser absorptivity, and the performance of the final parts, when comparing use of GA powder to use of WA powder as feedstock for AM [10,29].
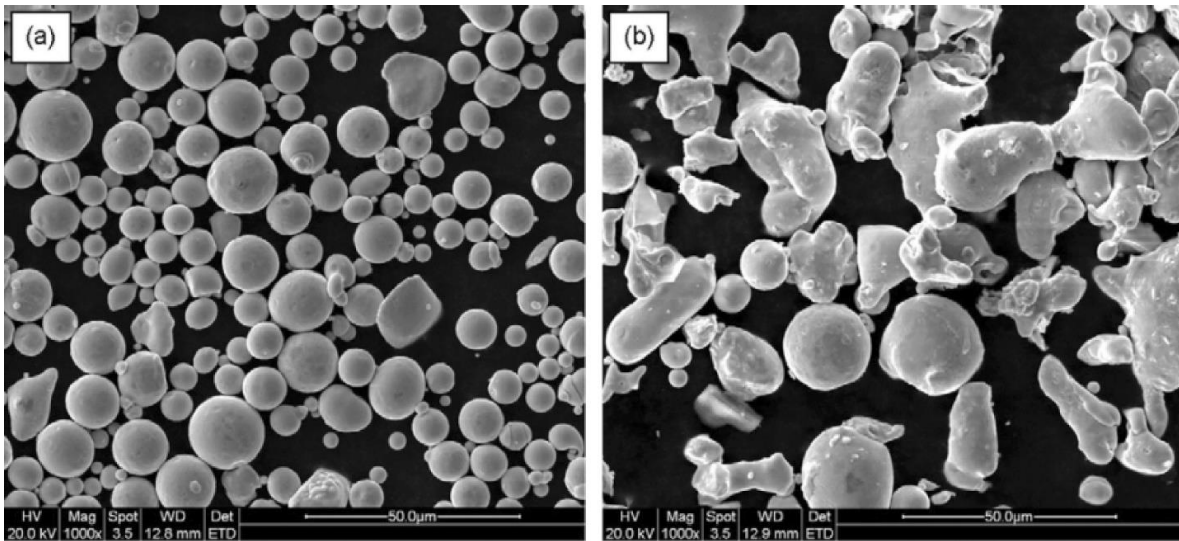
Figure 1.3: SEM images showing characteristic morphology of (a) GA powder (b) WA powder [11].

Irrinki et al. found that low energy density scanning parameters (64-84 J/mm^3) lead to a higher theoretical density and improved mechanical properties of parts made from SS 17-4 PH GA powders than those made from WA powders[30]. Figure 1.4 shows a representative image of the samples deposited by WA powders and used for tensile testing in this study. For example, the specimens made from GA powders using an energy density of 64 J/mm^3 exhibited an ultimate tensile strength of ~1020 MPa with 25% elongation and a hardness of 28 HRC; whereas, the specimens made from WA powders with an energy density of 64 J/mm^3 exhibited an ultimate tensile strength of ~460 MPa with 8.5% elongation and a hardness of 26 HRC. However, at high energy density scanning parameters (>104 J/mm^3), parts made from GA powder and WA powder exhibited similar properties [30]. For example,

the specimens made from GA powders using an energy density of 104 J/mm³ exhibited an ultimate tensile strength of ~920 MPa with 16% elongation and a hardness of 25 HRC; whereas, the specimens made from WA powders using an energy density of 104 J/mm³ exhibited an ultimate tensile strength of ~980 MPa with 14% elongation and a hardness of 36 HRC. An increase in the theoretical density from approximately 90% to 97% was observed in samples made from WA powder as the energy density increased from 64 J/mm³ to 104 J/mm³. Li et al. also found that SS 316L WA powder lead to a decrease in theoretical density of the final part compared to GA powder [11]. This was attributed to the higher oxygen content found in WA powders and the increased packing density of GA powders. However, the parts made from WA powder and the parts made from GA powder exhibited comparable mechanical properties when processed at high energy density, suggesting that irregular (i.e. non-spherical) morphology is adoptable in metal AM [2,30].
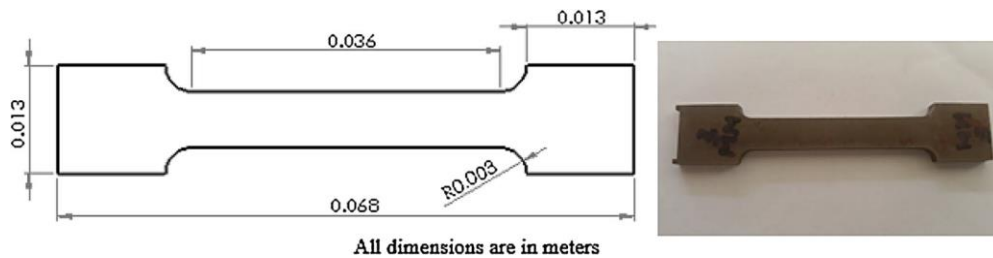
Figure 1.4: Geometry and and image of a part created by laser powder bed fusion using WA powder as feedstock.

Another powder production method, named as arc spraying, involves using a combination of thermal spray techniques and molten particle separation by counter gas flow. This arc spraying system has been studied as an alternative to GA powders in metal AM [31]. This method created near-spherical powders with little void content in small quantities when the counter gas was Argon. However, flattened particles with significant porosity were produced if air was used as the counter gas. While this method shows significant advances

in small scale powder production, it requires wire feedstock and temperatures beyond those required for gas atomization (e.g., 3700 to 4700 °C [31]). Typically, the feedstock powder is melted again in metal AM. This double melting represents a significant waste of energy and cost. To overcome the challenges, alternative and environmentally sustainable feedstock powders need to be explored. Pinkerton et. al. used machining chips as the feedstock material in metal AM to deposit thin walls [12–14]. The chips were sieved and only those with sizes below 425 μm were used in their study. They found surface oxides on the chips led to an increased corrosion rate in the final part [13]. The present work aimed to convert machining chips to powders first, and to investigate the usability of the powders created from the machining chips in metal AM.

Mechanical milling or high energy ball milling (HEBM) has also been utilized to produce powders for a variety of powder metallurgy techniques such as spark plasma sintering, hot isostatic pressing, and thermal spray [32–34]. Mechanical milling can tailor the morphology and the particle size of the powders by varying the milling conditions (details to be discussed in the next section) [35–39]. However, the primary objective of most of the past and current studies on mechanical milling was to improve the mechanical behavior of the materials and to investigate the strengthening mechanisms. There is evidence that a variety of initial feedstock, such as waste machining chips, can be reduced to particles sizes within the ranges appropriate for metal AM. Some studies on stainless steel have documented changes in morphology and particle size using different process control agents (PCAs) [36], and others have reported rocklike powders with particle sizes of 50-150 μm were fabricated after milling in Argon [39]. In addition, an increase in solid solubility of metallic element A in matrix B, exceeding the equilibrium solubility, has been achieved in

mechanical milling, particularly in cryomilling [40]. Thus, alloys of compositions otherwise unachievable can be created [33,40]. To make mechanical milling a viable option for metal AM feedstock, it is critical to understand the relationship between the processing parameters and the morphology, particle size, and chemical composition of the powder, which is challenging due to the complex interactions between the balls and feedstock during milling. Fundamentals of ball milling techniques are discussed in the following section.

1.2 Ball Milling

Mechanical milling breaks down coarse grained feedstock into nanostructured powders by severe plastic deformation [41,42]. The collisions between the balls, as well as the collisions between the balls and the inner wall of the container, result in mechanical force on the feedstock, which can be resolved to compressive stress and shear stress. These stresses plastically deform the feedstock and lead to a high dislocation density in the feedstock. The dislocations evolve into sub-grains and transform to high angle grain boundaries through a series of pile-up and annihilation events (Figure 1.5) [43]. Eventually grain refinement is achieved, which increases the yield strength of the powder via the Hall-Petch relation [44],

$$\sigma_y = \sigma_i + \frac{k_y}{\sqrt{D}} \qquad \text{Equation 1.1}$$

where D is the grain diameter, k_y is the Petch parameter, and σ_y and σ_i are the yield stress and the stress required to move a dislocation though the lattice, respectively.
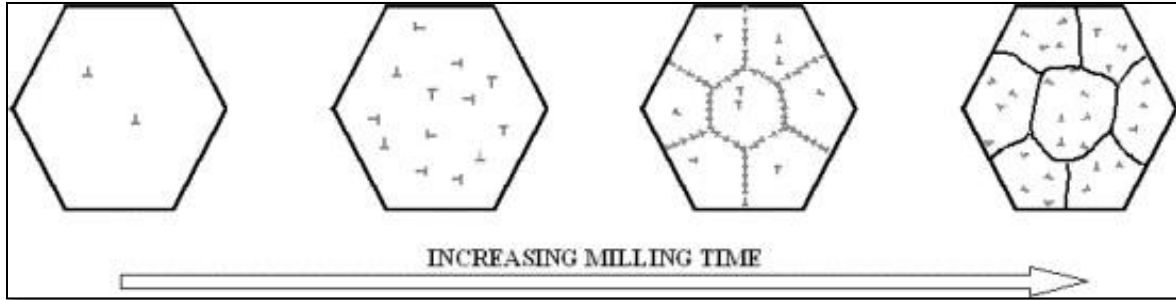
Figure 1.5: Schematic representation of grain refinement during ball milling [40].

The mechanical force also creates new surfaces while it decreases the particle size. However, cold welding occurs as the powder particles collide with the balls, or with other particles, and the wall of the container. Mechanical milling energy has been studied by several different models to reveal its role in refining particle size [45–49], refining grain size [50,51], and phase transformation in metastable austenitic stainless steels [39]. However, the relationship between milling parameters and morphology change of the powders is not yet fully investigated. Particle size refinement and morphology evolution are predominantly determined by the impact forces between the balls, walls, and other particles [50]. The refinement mechanism is influenced by the ball milling parameters such as process control agents (PCAs) [35,52], types of milling (wet or dry) [36], and temperature [40,41].

Shashanka and Chaira conducted planetary ball milling on duplex and ferritic steel powder with 8 mm diameter chromium steel balls in two conditions: one with the addition of stearic acid and the other without [36]. Both ball milling conditions used toluene as a wet milling media. Stearic acid was used as a process control agent (PCA) to reduce cold welding of particles during milling. Toluene also reduced the possibility of cold welding and oxidation [36]. The results of this paper indicate that the addition of stearic acid decreases the powder particle size faster and leads to a more flakey morphology (Figure 1.6a), compared to the ball

milling under the same parameters without stearic acid (Figure 1.6b) [36]. It is also worth noting that the morphology of the ferritic powder milled in the absence of stearic acid changed from flakey to rocklike as the powder changed from austenite to martensite after 10 hours of milling.

Enayati et al. also reported a phase transformation from austenite to martensite when stainless steel waste chips were ball milled in argon with 20 mm chromium steel balls for over 100 hours [39]. This study provided preliminary evidence that stainless steel powder could be created from scrap chips using planetary ball milling in an argon atmosphere. However, only one scanning electron microscopy (SEM) image was provided showing the powder had a rocklike morphology with a particle size below 100 μm (Figure 1.6c). No discussion was provided regarding the mechanism of morphology evolution from chips to powder and how the ball milling parameters affected the particle size reduction. Cast iron waste chips have also been converted to powder with a particle size less than 150 μm and with irregular/flakey morphology in 100 hours (Figure 1.6d) [38]. However, the processing parameters were not clearly explained in this study. It stated, "an alumina ball mill" and "a constant rotation of 60" were used. Nevertheless, the diameter of the balls and the initial chip size were not identified, not to mention the rationale of selecting these processing conditions.

Canakci and Varol investigated the morphology change of AA7075 (an aluminum-zinc-magnesium alloy) chips after planetary ball milling up to 10 hours [53]. A roller crusher was employed to refine initial coarse chips to smaller chips with a consistent size [53]. Subsequently, the fine chips were ball milled with an aggressive 30:1 ball-to-powder weight ratio, which enabled significant particle size reduction to occur within 10 hours. The

consequent powder exhibited irregular morphology (Figure 1.6e). However, the size and type of the balls were not mentioned in this paper. In a study by Yao et al., AA6063 (an aluminum-silicon-magnesium alloy) machining chips were crushed into granules and subsequently ball milled with SiC nanoparticles to create metal matrix composite precursor powder for spark plasma sintering [54]. Significant particle size reduction occurred in 12 hours using balls of 9.6-mm-diameter as the milling media and stearic acid as a PCA in the planetary ball milling. Particle size distributions of the powder was provided. However, the morphology evolution was not discussed.

　　According to the literature review discussed above, the existing body of the literature is lack of a complete fundamental understanding of the correlation between the evolution from chips to powders (including both particle size reduction and morphology change) and the selection of ball milling parameters, particularly the effect from ball size.
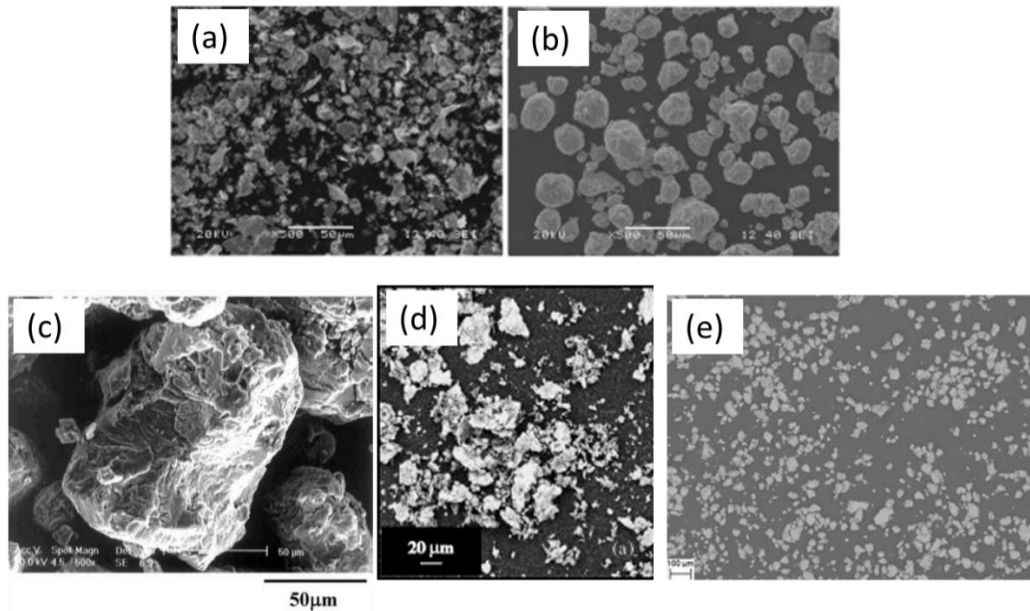
Figure 1.6: Morphology of ball milled powder reported by a,b) Shashanka and Chaira (with and without stearic acid, respectively) [36], (c) Enayati et al. [39], (d) da Costa et al. [38], and (e) Canakci and Varol [53].

On the other hand, several models for ball milling have been proposed to understand the energy transfer from balls to feedstock and how it is corelated to the properties of final powder [50,51,55]. Different approaches were explored to identify the ideal ball milling parameters for a desired outcome. These models can be grouped into two main categories: thermodynamic and Hertzian based impact. Both energy transfer models are dependent on the acceleration rate, size, and materials of the balls and feedstock. The individual interactions between balls and feedstock are also modeled according to the dimensions of the ball mill equipment, rotation speed, temperature dissipation, and Brownian-like motion.

Chattopadhyay et al. investigated the force per impact dependent on ball mill dimensions on the basis of Hertzian impact theory [51]. They concluded that the main disk speed had the most significant influence on radial force, and commented that the elastic modulus of the balls and jars should not be overlooked as it changes how the force per impact is transmitted to the powder [51]. Gusev and Kurlov estimated the motion of the balls and

13

correlated it to the reduction in particle size as a function of the mill dimensions, rotation speed, and ball diameter [50]. It was revealed that the change in acceleration rate of the balls and the force per impact varied as a function of the turn angle in a planetary ball mill [50]. Several studies note the relation between the fracture strength of brittle particles and particle size to determine that an increased stress is required to reduce the size of small particles [45,46]. *In-situ* imaging of the feedstock during milling was utilized to determine ball milling impact duration in some studies [47,49,56], while computer simulation was used in others [55,57]. Dallimore and McCormick used the distinct element method to simulate a two-dimensional model of ball motion. But they found that varying milling speed did not significantly affect the kinetics of the CuO/Ni displacement reaction propagation over the range of speeds that were investigated [55]. Desré related the required energy to transition materials from a nanocrystalline state to amorphous state by thermodynamic relations [58], and Trapp and Kieback determined the energy transferred to the powder through geometrical consideration by relating the contact radius and height differences before and after impact with powder [59].

While each of the aforementioned models provided insights into the correlation between the ball milling speed and the energy that was transferred to the feedstock from the milling media, few has given sufficient attention to the effects resulting from variances in ball dimensions, material properties of feedstock and balls, and stresses imparted on the feedstock. To establish a model that depicts morphological evolution of the feedstock during ball milling, these parameters must be considered.

1.3 Metal Recycling

Currently metal chips are recycled by sorting, melting, and casting/rolling into geometries that can be adapted by various processing techniques. Production of austenitic stainless steels has been reported to generate approximately 1.6 tons of CO_2 emissions for every ton of recycled stainless steel [60]. This is significantly less than the estimated 5.3 tons of CO_2 emissions generated from the production of virgin stainless steel [60]. However, the average end-of-life recovery rate of stainless steel is estimated at 80 wt.%, and the absolute losses of alloying elements to slag is substantial [61]. In other types of metals such as aluminum alloys recovery rates for traditional casting processes has been reported between 45-48 wt.% [53,62–65].

In terms of sustainability, retaining alloying elements by consolidation via severe plastic deformation (SPD) is an attractive alternative when compared to the losses associated with melting metal waste. Several attempts have been made to recycle aluminum machining chips by compressing and extrusion. However, this consolidation technique is limited to parts with a constant cross section [65]. To produce complex parts from metal scrap chips, it is proposed to mechanically mill chips into a powder suitable for metal AM.

1.4 Motivation and Objectives

Literature review on metal AM and ball milling, as discussed in the previous sections, elucidated the following points. (1) Both spherical powders such as GA powder and irregular powders such as WA powders have been successfully utilized as feedstock for metal AM. The mechanical properties of the 3D components made from these two types of feedstock powders are comparable to each other. (2) The properties and performance of the components made by AM significantly dependent on the characteristics of the feedstock

powder. Generally, the desired characteristics of the feedstock powder include high flowability and packing density which is found in powders with spherical morphology, low fractions of satellite particles, and narrow particle size distributions. (3) Machining metal waste is typically recycled via melting and casting/rolling, which lead to detrimental environmental impacts such as CO_2 emission, energy consumption, and material losses due to oxidation at high temperatures. (4) Ball milling technology has been commonly used to improve the mechanical properties of the materials and the relevant strengthening mechanisms have been investigated. Recent studies also show that ball milling can convert metal machining chips to powders. The particle size and the morphology of the powders can be tailored by varying some ball milling parameters such as milling speed, ball diameter, ball-to-powder weight ratio, and temperature.

In spite of the progresses in processing optimization and product property improvement that have been achieved, metal AM still faces several challenges due to low feedstock utilization efficiency and the availability of ideal feedstock powders. One environmental challenge of using GA or WA powder in metal AM is the high energy consumption required to produce the powder through atomization. Pure metals such as Al, Cu, Fe, Ti and Ni, or sometimes simple binary alloys such as Al-Mg, are used in ingot form as the starting material for atomization. The ingot is melted, and powder is created when the molten metal is sprayed through the atomization nozzles. The phase transformation during melting requires energy to account for the enthalpy difference between the liquid and solid states [66]. The energy input represents a major fraction of the energy consumption for heating and melting metals. As an example, to heat one kilogram of iron from room temperature to 1350 °C, the amount of energy required is 6.10×10^5 J, whereas to heat one

16

kilogram of iron from room temperature, then melt it and then heat the liquid to 1580 °C, which is the typical required temperature for casting iron, the amount of energy required is 1.49×10^6 J. The latter is about 2.4 times the former, and the major reason for this vast difference is the large amount of heat required to melt iron, which is 7.76×10^5 J/kg [67]. Typically, the feedstock powder is melted again in metal AM. This double melting represents a significant waste of energy and cost. To overcome these challenges, the primary objective of this work is to create alternative and environmentally sustainable feedstock powder for metal AM. The primary criteria to produce alternative feedstock powder for metal AM include acceptable morphology, chemical composition, and controllable particle size distribution [6].

Mechanical milling presents a potential opportunity for sustainable powder production because it can break down a variety of starting materials with different initial sizes into powder particles, as discussed in Section 1.2. However, a thorough understanding of the evolution from chips to powders (including both particle size reduction and morphology change) and the selection of ball milling parameters, particularly the effect from ball size, is hindered by the complexity of the ball-powder interactions during milling. To provide insights into this evolution, one goal of the present study is to formulate an analysis of the impact force on a powder particle and the consequent maximum deformation depth during ball milling. In addition, the theoretical analysis was used in conjunction with several mechanical milling tests to create powders suitable for metal AM from metal machining waste. 304L stainless steel was selected as the model material due to its wide use in AM for various structural materials [68]. 304L stainless steel is desirable for metal AM because of its high strength, high weldability, and corrosion resistance [69]. Also, 304L was selected to

17

investigate the effectiveness of ball milling on materials with high alloy content (Cr >10% in weight).

To create powder suitable for use in metal AM, a novel approach of changing balls diameter during ball milling was proposed. Various ball milling procedures were implemented to experimentally investigate the effect of ball diameter on the powder morphology evolution and particle size refinement. The detailed experimental approach and procedures are discussed in CH 2. A theoretical analysis was performed to evaluate the impact force on powder and the consequent maximum deformation depth per impact during ball milling with different ball diameters, the results of which is included in CH 3. The powders experimentally created from metal waste via ball milling were characterized in terms of morphology, particle size, and microstructure. The relevant results are discussed in CH 3. It is found that a dual-stage ball milling strategy effectively converts machining chips to powder with desirable characteristics (near spherical morphology with particle sizes of 38-150μm) for metal AM. To verify the feasibility of using the milled powder in AM, single tracks were successfully deposited using laser engineered net shaping (LENS®) and compared to the single tracks that were deposited from GA powder using identical LENS® processing parameters. Characterization of the single tracks including microstructure, melt pool geometry, and composition will be provided in CH 4. The changes of nanoindentation hardness in both powder and single tracks will also be discussed in CH 4. Finally, summary of this work will be discussed in CH 5 and future work is proposed.

Chapter 2   Approach: Experimental   Procedure   and Characterization Methods

This chapter is to describe the experimental procedure and characterization methods that were used in this work. Ball milling of stainless steel machining chips was performed to fabricate alternative feedstock powders for metal AM. Various ball milling conditions were implemented to investigate the effect of ball diameter on the powder morphology evolution and particle size refinement. Selection of initial processing parameters is justified. The powders collected at different stages of the ball milling procedure were characterized in terms of particle size distribution, morphology, phase constitution, and nanoindentation hardness. For comparison purpose, GA powders of similar chemical compositions were characterized as well. Both GA powder and the ball milled powder created from machining chips were used in laser engineered net shape (LENS®) deposition to make single tracks, with equivalent deposition parameters. The geometry, microstructure and hardness of the single tracks are characterized via optical microscopy, scanning electron microscopy (SEM) combined with electron back scattering diffraction (EBSD) and energy dispersive spectroscopy (EDS), and nanoindentation.

2.1   Material Selection

304L stainless steel was selected as the model material due to its wide use in AM for various structural materials [68]. 304L stainless steel is desirable for metal AM because of its high strength, high weldability, and corrosion resistance [69]. Also, 304L was selected to investigate the effectiveness of ball milling on materials with high alloy content (Cr >10% in weight).

The material used in the present study was provided by AK steel (West Chester Township, Butler County, Ohio, OH). To produce chips, stacks of 25x100x1 mm^3 rolled SS-304L samples were placed on end and machined using a conventional mill without coolant. The chemical composition of the chips is provided in Table 2.1. The individual chips had serrations along the length (5-20 mm) due to the previous machining operation as shown in Figure 2.1. Approximately 300 µm serrations extended more than ¼ of the thickness (300-500 µm) of the chips. Stainless steel chips were cleaned by mixing with ethanol for 20 minutes to reduce contamination from machining and collection, followed by air drying.

Table 2.1: Nominal chemical composition of stainless steel machining chips

Elements	Fe	Cr	Ni	C	Mn	Cu	Si	Mo	V
wt.%	Balance	18.18	8.09	0.0253	1.30	0.57	0.41	0.26	0.064
Elements	W	N	P	Nb	Al	B	S	Ti	Ca
wt.%	0.059	0.038	0.027	0.013	<0.003	0.0026	0.0021	0.002	<0.0005
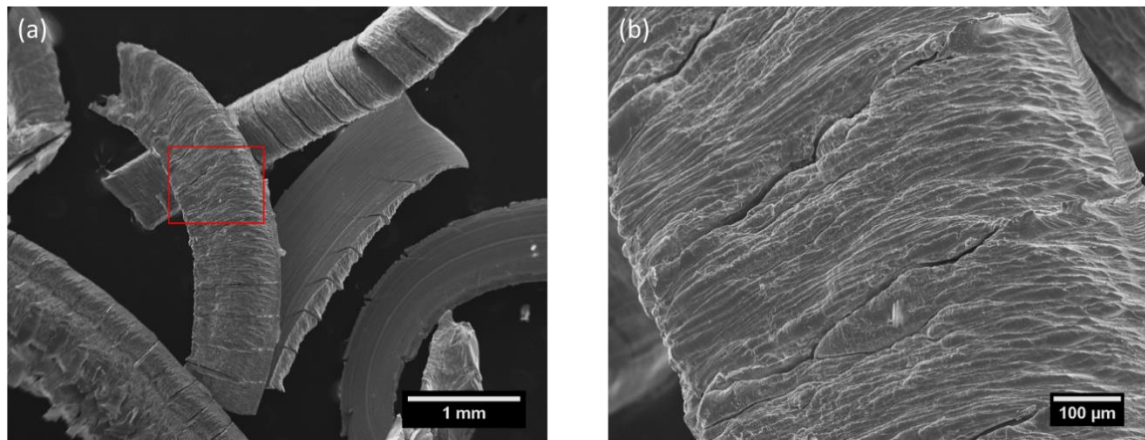
Figure 2.1: (a) Representative SEM image of stainless steel machining chips at low-magnification. (b) Surface morphology of machining chips in the boxed area in (a) at a high-magnification.

2.2 Ball Milling Procedure

High energy ball milling was employed to create powders from waste chips. The processing parameters, such as ball diameter and milling time, were varied to tailor the

morphology and particle size of the powder, as well as to increase the yield of the powder. Various ball milling equipment, parameters, and methods and their effect on feedstock are discussed in this section. A novel dual-stage milling procedure is outlined.

2.2.1 Categories of Ball Milling

There are several types of ball mills that are commonly used at lab/research scale, including planetary, attrition, roller, 1D vibratory, and 3D vibratory (Figure 2.2) [70]. A planetary ball mill consists of multiple jars spinning on their respective axis, and on a common axis similar to how planets orbit the sun [42,70]. Attrition mills spin a rod within a stationary container to induce collisions between the rods, balls, and feedstock [40,71]. A roller mill spins a cylindrical container such that it only uses gravity to induce collisions between the milling media (a large ball or a cylindrical rod) and feedstock [71]. 1D and 3D vibratory mills are similar as they violently shake balls and feedstock, but 1D vibratory mills only shake along one direction as opposed to 3D vibratory mills which shake in three directions [42]. Each of these mills has advantages and disadvantages associated with the way they impact the balls.
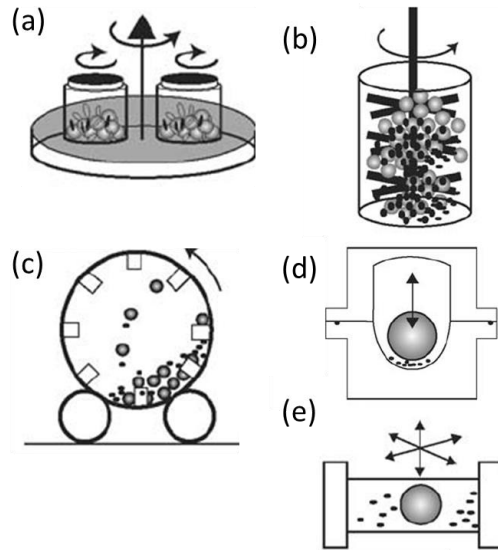
Figure 2.2: Different types of ball mills: (a) planetary mill, (b) attrition mill, (c) roller mill, (d) 1D vibratory mill, and (e) 3D vibratory mill [70].

Attrition mills can be adapted more readily to use a constant flow of liquid nitrogen either in contact with the feedstock or within a cooling jacket as the milling container is stationary, but the collision force between the balls and the feedstock varies widely from the center to the edges of the mill [42]. All other mills have moving containers which makes temperature regulation more of a challenge. Vibratory mills often reduce particle size and grain size quickly by violent shaking, but they are difficult to use with a large quantity of feedstock [42]. Roller milling in small quantities with small diameter cylinders do not have enough distance where the balls can gain sufficient momentum to refine particle size and grain size effectively (as impacts are driven by gravity), but large diameter mills can efficiently reduce particle size and grain size [71]. Planetary ball mills offer higher impact forces than small diameter roller mills, more consistent impact velocity than attrition mills, and a higher volume than vibratory mills to accommodate more feedstock [51,56,70,72]. However, temperature regulation is an issue planetary ball mills face, and they are often run

22

on a duty cycle to accommodate the buildup of heat caused by friction within the mill. The excess heat can be detrimental to particle size reduction as it leads to increased cold welding of particles, agglomeration, and decreased yield of collected powder [45].

Due to the issues associated with non-uniform impacts in attrition mills, small powder yield of vibratory mills, and low impacting forces of roller mills at lab scale, planetary ball milling is often used by researchers. A planetary ball mill (shown in Figure 2.3) was chosen for the ball milling of waste chips for the following reasons: (1) to ensure comparable parameters and results to current research, (2) to maintain consistent impacting forces, and (3) to obtain a sufficient quantity of powder for subsequent use in metal AM. In addition, an attrition cryomill was used to study the effect of cryogenic temperature on the evolution from chips to powder when the stainless steel chips were ball milled in liquid nitrogen.

Figure 2.3: Planetary ball mill and milling jars used for mechanical milling of stainless steel chips.

2.2.2 Milling Environment

Ball milling is done in a variety of gasses and liquids depending on the materials and the intended applications. Ball milling of titanium, for example, requires an inert environment during milling to prevent spontaneous oxidation of new surfaces [73].

Commonly, ball milling is done in readily available media such as air, argon, water, ethanol, or liquid nitrogen (LN_2). LN_2 is often used as an inert environment that prevents combustion of volatile powders and cold welding of particles. The cryogenic temperature due to LN_2 also suppresses dislocation annihilation so that the dislocation density is increased in the materials. When the feedstock is in direct contact with LN_2, some materials, such as aluminum and iron, tend to form metal nitrides during cryomilling, which is beneficial to the stability of ultrafine grained structure by pinning grain boundaries and also contributes to strengthening [40]. Argon gas is often used at room temperature to prevent oxidation of newly milled surfaces, while water and ethanol are used to prevent excess cold welding of particles [35,36,39,42]. Sometimes, a combination of argon in direct contact with the milling materials and a container cooled by LN_2 is used to maintain an inert atmosphere preventing contamination and to provide cryogenic temperatures to suppress dislocation annihilation [74–76].

While ethanol, liquid nitrogen, and water are commonly used to prevent cold welding by maintaining temperature, small amounts of process control agents (PCAs) can also be used. PCAs are generally organic compounds used to reduce cold welding and prevent agglomeration. While the reduction of cold welding is beneficial for particle size refinement and powder yield, PCAs often introduce contamination, particularly hydrogen, which requires a post milling process known as degassing to remove. However, these trapped gasses can lead to porosity which is detrimental to mechanical properties and causes excess spattering in metal AM applications [40,41,77,78]. To prevent contamination from processing atmosphere and PCAs, planetary ball milling was performed in jars containing Argon in the work presented here. To reduce cold welding due to increased temperatures, a

duty cycle of 5 minutes on and 5 minutes off was used throughout all experiments. This time interval was chosen by observation of several experiments with increased agglomeration and cold welding at longer "on" cycles. A smaller portion of testing also used both ethanol and liquid nitrogen to observe the effects of milling in different environments.

2.2.3 Milling Parameters

Several milling variables can be manipulated in a planetary ball mill to increase the energy transfer rate from the balls to the feedstock [42,47,50–52,55,56,72]. The rate of energy transfer is primarily influenced by the main plate rotation speed and ball-to-powder ratio [55,72]. The main plate speed determines the frequency of the collision between the balls and the feedstock and container, while the ball-to-powder weight ratio directly affects the amount of energy transferred to the feedstock per rotation [58]. To reduce particle size rapidly, a high energy transfer rate is desired [58]. In contrast, the method chosen to control the energy transfer per impact determines the morphology of the powder, and must be considered to reduce cold welding of particles [50]. While the main plate rotation rate changes the frequency of impacts, the diameter of the main plate and container determine the velocity of the balls at impact [50]. This velocity combined with the mass and material properties of the balls determine the energy transfer per impact [50]. To quickly reduce particle size and create a more spherical morphology, a main plate speed near the maximum was used along with different ball sizes for different feedstock with various initial sizes.

The machining chips were milled using a PQ-N04 planetary ball mill (Across International, Livingston, NJ) in cylindrical stainless steel jars of 52 mm inner diameter. The center of the jars is 85 mm from the center of the main plate. Stainless steel balls of 20 mm diameter and 6 mm diameter, denoted as Φ-20 balls and Φ-6 balls, were used with a

consistent 15:1 ball-to-powder weight ratio. 50-60% of the jar height was filled with the balls. The rotation of the main plate and the jars was maintained at 500 RPM. Five minutes on/five minutes off cycles were applied to prohibit over-heating of the balls. To reduce surface oxidation, an argon environment inside the jars was maintained by sealing the jars inside a glovebox with less than 1 ppm oxygen content. Both milling time and ball diameter were varied to investigate the effect of the ball milling conditions on the powder morphology evolution during milling. Four ball milling conditions were studied: BM-20-60hr, BM-6-60hr, an interrupted (BM-2Stg-Int-60hr), and an uninterrupted dual-stage milling approach (BM-2Stg-60hr). Sample identification is provided in Table 2.2, where BM indicates ball milled powder, followed by the diameter of the milling balls (2Stg stands for dual-stage milling with both Φ-20 balls and Φ-6 balls); "Int" denotes an interrupted operation, and the final number is the total milling time. The interrupted dual-stage milling means the ball milling process was stopped at 12-hour intervals to collect the powder to investigate the morphology evolution.

Table 2.2: Sample ID of 304L stainless steel

Powder

Sample ID	Powder Process	Time Milled (hour)	
		Φ-20 balls	Φ-6 balls
BM-20-60hr	Ball Milled	60	0
BM-6-60hr	Ball Milled	0	60
BM-2Stg-60hr	Ball Milled	24	36
BM-2Stg-Int-24hr	Ball Milled	24	0
BM-2Stg-Int-36hr	Ball Milled	24	12
BM-2Stg-Int-48hr	Ball Milled	24	24
BM-2Stg-Int-60hr	Ball Milled	24	36

Single Tracks

Sample ID	Powder Feedstock	Deposition Variables	
		Laser Power (W)	Scanning Speed (Inches per minute)
ST-GA-460-40	Gas Atomized	460	40
ST-GA-410-40	Gas Atomized	410	40
ST-GA-360-40	Gas Atomized	360	40
ST-BM-460-40	BM-2Stg-60hr	460	40
ST-BM-410-40	BM-2Stg-60hr	410	40
ST-BM-360-40	BM-2Stg-60hr	360	40

2.2.4 Other Ball Milling Strategies

Several other ball milling procedures were used to refine chips with a thicker and more uniform cross section. These thicker chips were machined using a technique known as nibbling. These chips were made from the same starting plate material (304L stainless steel) described previously. But these thick chips do not exhibit serrations, as shown in Figure 2.4. To refine these thick chips, several milling procedures were used including cryomilling,

planetary ball milling in ethanol, and planetary ball milling in argon. The effectiveness of each of these milling procedures was compared with the effectiveness of milling GA 316L powder (44-150 micron). 44-150 μm GA 316L powder was supplied from Carpenter Powder Products. The composition of this powder is given in Table 2.3. Each of these methods are outlined below.
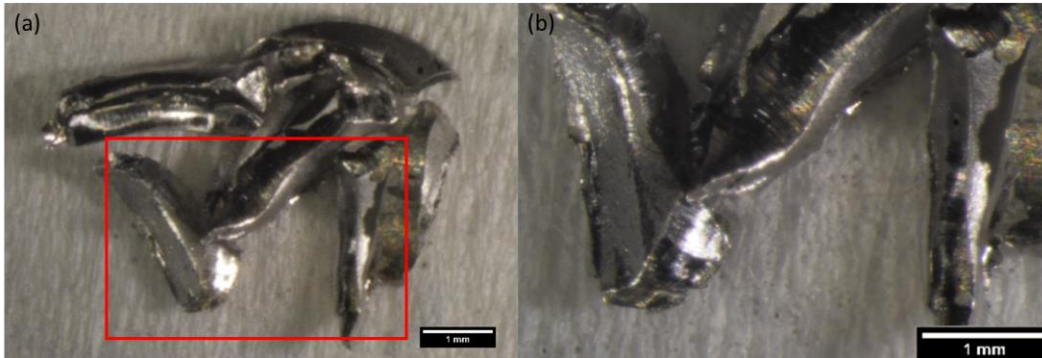
Figure 2.4: (a) Representative optical image of thick stainless steel machining chips at low-magnification. (b) Surface morphology of machining chips in the boxed area in (a) at a high-magnification.

Table 2.3: Nominal chemical composition of GA 316L

Elements	Fe	Cr	Ni	C	Mn	P	Si	Mo
wt.%	Balance	16-18	10-14	0.03	2.00	0.045	1.00	2.00-3.00

Cryomilling of both GA 316L powder and 304L thick chips was performed in a MSK-SFM-3LN liquid Nitrogen cryogenic rotor mill (Figure 2.5) for 8 hours with Φ-6 and Φ-20 balls, respectively. The flow of liquid nitrogen was regulated by placement of a thermocouple near the top of the vacuum insulated tank. The container made from stainless steel has dimensions of 210 mm diameter and 180 mm height. The stainless steel mixing blade rotated at a constant rate of 350 RPM. The mixing blade consists of a 20 mm main shaft with three 8 mm spindles spaced 30 mm apart. The mixing blade provides the velocity for impacts

between the balls, container, and the feedstock. However, it also impacts the feedstock and contributes to particle size refinement.

Figure 2.5: Cryogenic ball mill and milling container.

Ball milling was performed with and without ethanol on the thick chips and GA 316L using a PQ-N04 planetary ball mill as described in the Section 2.2.1. Ethanol is often used as a PCA to prevent cold welding of particles during milling [42,52,70]. To achieve the maximum energy transfer rate, the rotation of the main plate and the jars was maintained at 500 RPM. Stainless steel balls of Φ-20 and Φ-6 were used as the balls with a consistent 15:1 ball to powder weight ratio. Initial particle size reduction of the thick chips was performed by milling with Φ-20 balls for 96 hours, followed by particle size reduction and morphology modification using Φ-6 balls for 36 hours. A small amount of powder was collected at various stages of the milling cycle to observe morphology evolution. To study the effect of feedstock properties on morphology evolution, GA 316L powder was milled with Φ-20 balls in argon for 12 hours and Φ-6 balls in ethanol for 12 hours 50-60% of the jar volume was filled with the balls. In the tests performed with ethanol, feedstock and balls were submerged in 50 mL

of ethanol. Five minutes on/five minutes off cycles were applied to prohibit over-heating of the balls and ethanol.

2.3 Characterization of Chips and Powders

The powder was characterized by sieving, scanning electron microscopy (SEM) and X-ray diffraction (XRD). Because of the small length scales associated powder feedstock (<150 µm), traditional mechanical characterization methods are not feasible. Thus, the hardness and modulus of the powders were tested by nanoindentation. While these characterization techniques help us to determine the particle size, morphology, phase constitution and mechanical properties, other properties such as laser absorptivity characteristics must be determined by deposition via metal AM. Each characterization method and its use in this work are described in this section.

2.3.1 Particle Size

Particle size distribution can be determined in several ways: measuring particles from SEM images or optical microscopy images, sieving, or laser diffraction [2,79]. However, each method has limitation. Imaging approaches only image one side of the particle, and depth of the particle can only be qualitatively determined [2]. Laser diffraction equipment is expensive, but this technique uses the volume of the particle instead of the cross-sectional area and relates it to an equivalent sphere with the same volume [30,79]. Sieving, another common approach, uses meshes with progressively smaller holes that allow only particles below a certain size to pass through [26]. The weight of the powder is then measured from each container and a particle size distribution can be determined. However, long slender particles can reorient themselves through the small openings given enough time [2].

To remove the powder with particle sizes outside the range of 35-150 μm and maintain a distribution of particle sizes ideal for LENS®, powder collected after ball milling was sieved for 15 minutes through 100, 140, 200, and 400 mesh sizes (150 μm, 106 μm, 75 μm, and 38 μm respectively). Powder was agitated using a Ro-Tap to maintain consistent shaking between each milling cycle. Particles less than 150 μm were removed from the ball mill during interrupted runs to study the morphology. To determine the accuracy of the particle size measurements, particle morphology was also studied.

2.3.2 Morphology

A simple and effective measurement of the aspect ratio of powder can be used to quantify the morphology of powder. A more spherical morphology is commonly preferred in metal AM to increase the ease of flow through the equipment and to increase the packing density of the powder [2,10,11]. To observe morphology development during ball milling, powder between 106-150 μm imaged in a JEOL JSM-6500 FE SEM with an acceleration voltage of 15kV at various stages of the milling process. The longest and shortest distances through the center of the particle were measured via ImageJ. To determine the sphericity of the milled powder, the average aspect ratio of 100 particles were measured across 10 separate images. The average aspect ratio, as well as the 30th, 50th, and 80th percentile (denoted as D30, D50, and D80, respectively) of aspect ratio were quantified.

2.3.3 Phase Change

XRD was used to qualitatively characterize phase change of stainless steel during ball milling. Several studies have identified stress induced phase change to martensite in metastable austenitic stainless steels [39,80–85]. The XRD patterns of the milled powder were compared to the as-received chips and GA powder. XRD of samples was performed

31

between 35°-105° 2θ at increments of 0.02° 2θ and a dwell time of 1 sec at each increment on a Bruker D8 Discover DaVinci Powder X-ray Diffractometer. Samples were spread evenly on a silicon single crystal plate using a glass microscope slide to avoid diffraction patterns of the substrate. The silicon single crystal plate is cut such that there is no background noise from 2θ in the range of 20°-120°.

The change of phase from austenite to martensite is particularly important as it increases the hardness [39]. As the powders hardness increases, the resistance to further plastic deformation also increases. An increase in the resistance of plastic deformation will influence the particle size reduction rate, morphology evolution, and cold welding of the powders [45,48,50,51].

2.4   Deposition and Characterization of Single Tracks

Typically, parameter optimization of new materials used in metal AM starts with the deposition of single tracks. Single tracks are a line of powder solidified by the laser that give insight into ideal scanning parameters such as energy of the laser, scanning speed, and material deposition rates. Characterization of the continuity and penetration can be done by optical imaging similar to the method shown in Figure 2.6. Distortion and irregularity are found in single tracks with low energy density and slow scanning parameters [86,87].
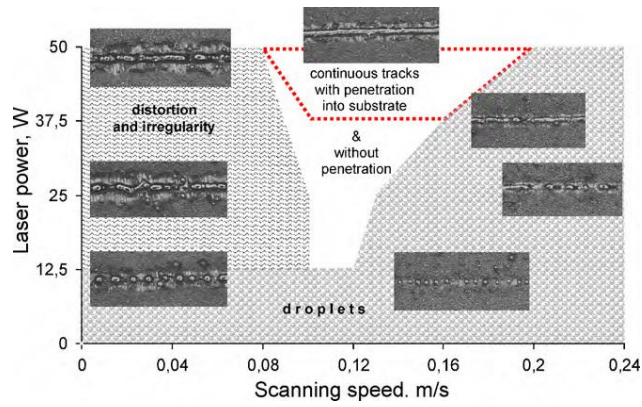
Figure 2.6: Single track process map identifying the ideal zone of parameters for 316L powder feedstock [86].

The cross section of the single tracks is often investigated to determine if the single tracks show sufficient penetration (Figure 2.7). The cross-sectional microstructure also identifies vaporization induced porosity as indicated by the arrows in Figure 2.7. Bead up of the single tracks is often observed at fast scanning rates, when the powder is re-melt while the substrate is not [88].
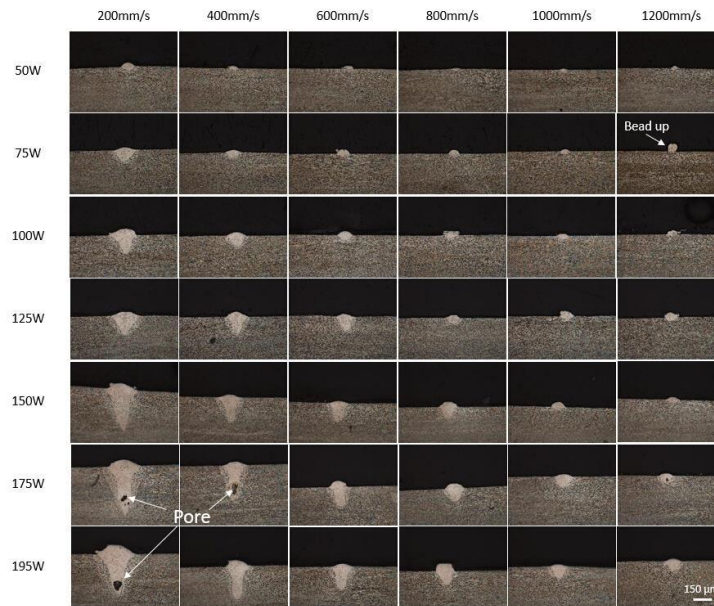
Figure 2.7: Cross-sectional melt pool profile of single tracks made from Ti-6Al-4V powder [88].

33

The surface finish of parts made by metal AM depends on the uniformity of the melt pool and the absence of spattering [2,86,88]. Uniform melt pool and absence of spattering can be controlled in part by the scanning parameters, but also depends on the feedstock properties [10,11,89]. When the laser energy is above the ideal range, single tracks exhibit vaporization induced porosity; when the laser energy is below the ideal range, unstable or discontinuous melt pools form [86,88]. Entrapped gasses in feedstock can also lead to increased porosity and spattering as the gasses attempt to escape the melt pool [2]. The effect of laser power on ST-BM as compared to ST-GA are outlined in this section.

2.4.1 Deposition

Single tracks were deposited using an Optomec® 750 LENS powder feed system in powder bed mode. Instead of injecting the powders through the nozzles, a powder bed was created on the substrate by spreading powder between two 150-μm-thick spacers with a straight edge. The working distance of the laser (wave length = 1070 nm) was 0.340 inch from the surface (0.05 inch under focused), and the enclosure was maintained below 10 ppm oxygen. The primary gas in the enclosure was argon.

To study variation of laser power within the stable melt pool regime, a scanning speed of 40 inches per minute was used with laser powers of 360 W, 410 W, and 460 W to deposit ST-BM and ST-GA. ST-GA and ST-BM were 15 mm in length, spaced 2.5 mm apart, and approximately 1 mm in width.

2.4.2 Optical Characterization

Single tracks were imaged using an optical microscope. Adequate adhesion, uniform melt pool geometry, continuity, and minimal splatter can be determined by optical microscopy [2,86,88]. Continuity of single tracks verifies the laser power is sufficiently high

to consolidate the entire line of powder [88]. A uniform melt pool and minimal splatter leads to higher resolution in final print geometry, while adequate adhesion is required to have good strength [86,88–90].

One other way to quantify the consolidation behavior of single tracks is to measure the width of the single track. A wider single track is often made using a higher laser power, but melt pool geometry will also affect the final single track width [29,88,91]. A circular melt pool geometry with the same laser power will make a melt pool with a flat and wide profile when compared to a tear drop shaped melt pool, and a tear drop shaped melt pool will have a higher and more prominent ridge and a thinner profile [91].

2.4.3 Sample Preparation

Sample preparation for electron backscatter diffraction (EBSD) is critical for accurate characterization [68,92]. To increase the reliability of the results gathered in EBSD characterization, minimal lattice distortion due to final polishing is recommended [92]. Often, electropolishing is preferred as it minimizes mechanically induced deformation, but mechanical polishing can give optimal results when preformed carefully [92].

Single tracks were cross-sectioned using electrical discharge machining (EDM). They were then ground using SiC paper of 600, 800, and 1200 grit sizes on an eight-inch grinding wheel spinning at 200 RPM for 10 min at each step. An optical microscope was used to verify the removal of previous deformation at each step. Polishing was then performed by hand using 3 μm, 1 μm, 0.25 μm, and 0.05 μm polycrystalline diamond media suspension for 15 minutes, 15 minutes, 30 minutes, and 4 hours, respectively. Between each step of grinding and polishing, the sample surface was cleaned using DI water and soap to remove previous

polishing media. After the final polishing step, cleaning with DI water and a fluffed cue tip was performed to remove any excess residue.

2.4.4 Microstructure Characterization

Single tracks made with varying laser power and stable melt pools exhibit varying grain growth tendencies [93,94]. These differences in grain growth correspond to altered material properties [93,94]. In connection, it has been shown that metal AM parts exhibit anisotropic behavior parallel and perpendicular to the build directions [2]. Morphological anisotropy is exhibited by preferentially elongated grains regardless of lattice orientation whereas textural anisotropy is caused by preferred lattice orientation of grains. In previous studies, single tracks made with higher laser power and a constant scanning speed exhibited more columnar grain structure [68]. In a study by Gu and Jia an increase in laser energy density caused a change from coarse columnar dendrites to slender columnar dendrites [95]. These studies identify the need for characterization of ST-BM and ST-GA by EBSD.

Several key characteristics of single tracks can be identified by EBSD including grain size, grain orientation, and grain shape [93]. EBSD characterization is performed by using a SEM to accelerate electrons towards the sample, and capture information about the angle with which electrons backscatter off the surface of the sample [92]. A JEOL JSM-6500 FE SEM was used in conjunction with a DigiView EBSD Camera at 15 kV acceleration voltage with a step size of 1.5 μm. The EBSD software was set to index austenitic and martensitic lattice orientations. Average confidence index of individual crystal plane identification exceeded 0.5.

Void content of parts made from metal AM is the main cause for decreased material properties such as yield and ultimate strength [10,11,30]. Void content in metal AM can be

caused by porous feedstock powder [2]. Increased feedstock porosity can also lead to increased spattering as the entrapped gasses escape the melt pool [2]. To quantify the void content of single tracks, SEM imaging of cross-sectioned single tracks was performed using a JEOL JSM-6500 FE SEM. The quantification of pores was performed on each single track using ImageJ analysis of 10 high magnification images.

Energy dispersive X-ray spectroscopy (EDS) was also used to quantify the elemental composition of the deposited single tracks and verify homogeneity. EDS mapping of approximately 100 x 100 μm regions was used to determine the homogeneity of the single tracks. A JEOL JSM-6500 FE SEM was used in conjunction with an Oxford Instruments Max 80 SSD EDS detector at 15 kV acceleration voltage, using a pulse processing time of 6 to achieve a dead time below 35%.

2.5   Nanoindentation Testing

Nanoindentation technique is applied to characterize the hardness of the GA powders and ball milled powders that were fabricated in this work. Nanoindentation provides quantitative mechanical characterization (hardness, elastic modulus, wear, friction, etc.) of various materials, including bulk materials, coatings, thin films, and powders, at scales from nanometer to micron. Its capability of testing the mechanical properties of powder samples is particularly important to this work. A Hysitron ® TI Primer nanoindentation system with an anti-vibration table and enclosure (Figure 2.8) was used in the current work. This equipment provides a maximum load of 10 mN with a resolution of 1 nN and a maximum displacement of 5 μm with a resolution of 0.04 nm. This sensitivity combined with anti-vibration enclosure enable accurate measurements of hardness and modulus of materials even when the indents are less than 100 nm deep. A Berkovich diamond probe (TI-0039

Berkovich, 142.3º total included angle, 100nm tip radius) was used across all indentation tests. The hardness of each material was measured to investigate the relationship between processing and powder properties. The modulus values were used to verify consistent testing between samples. To obtain reliable data for hardness and modulus, tip area function calibration is performed on a standard sample (fused quartz) that has a consistent modulus and known Poisson's ratio.

Figure 2.8: Hysitron TI primer nanoindenter

The chips and powder were indented with a max load of 1 mN with a loading time-hold time-unloading time profile of 10s-15s-10s, while the single tracks were indented with a max load of both 1 mN and 5 mN. The 1 mN max load indents were performed using the same loading profile as used on the chips and powder; the 5 mN max loading profile was performed using a loading-hold-unloading profile of 50-75-50 to maintain the same strain rate. Hardness is calculated by dividing the max load (P_{max}) by the projected contact area (A) at that load, as defined in Equation (2.1) [96]. Figure 2.9 shows a typical load-penetration depth (p-h) curve obtained from nanoindentation testing. The slope of the unloading curve

(highlighted by an arrow in Figure 2.9), known as stiffness (S), is used to determine the

modulus and project the depth of plastic deformation. Subsequently, the contact area and

hardness are calculated from the tip area function. Calculation of the reduced modulus, E_r,

does not require plastic deformation to occur on the sample. E_r is calculated from the

stiffness and the contact area based on Equation (2.2) [96]. The reduced modulus can be

converted to the elastic modulus of the sample using the modulus of the indenter and the

Poisson's ratio of both the indenter and the sample, as defined by Equation (2.3).

$$H = \frac{P_{max}}{A}$$ **Equation 2.1**

$$E_r = \frac{S\sqrt{\pi}}{2\sqrt{A}}$$ **Equation 2.2**

$$\frac{1}{E_r} = \frac{(1\text{-}v^2)}{E} + \frac{(1\text{-}v_i^2)}{E_i}$$ **Equation 2.3**

where H is the hardness, P_{max} is the max load, A is the projected contact area, E_r is the

reduced modulus, S is the stiffness, E is the modulus of the sample, E_i is the modulus of the

indenter, v is the Poisson's ratio of the sample, and v_i is the Poisson's ratio of the indenter.
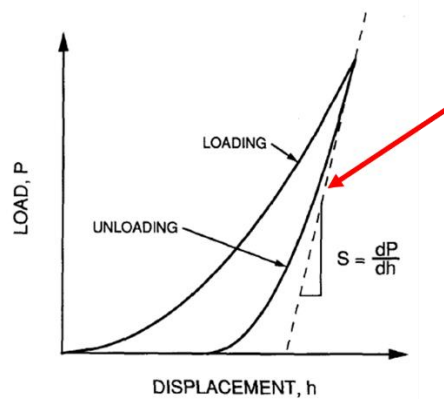
Figure 2.9: Typical load-penetration depth (p-h) curve obtained from nanoindentation testing. Red arrow pointing to the slope obtained from the unloading curve [97].

To avoid the plastic deformation zone and strain caused by the previous indents, it is

necessary to measure the longest distance of the plastic deformation and space indents away

from each other with a distance more than 5 times of this length. Scanning probe microscopy (SPM) was used to quantify this length. SPM images are produced by rastering the Berkovich tip across the surface using a piezo electric scanner. This information was also used to verify the roughness of the sample was less than a tenth of the indentation depth.

Powder and milling chips were mounted using a cold-mount epoxy resin system, and the cross section of single tracks were mounted in conductive material via metallographic specimen hot mounting. Each sample was then ground using SiC paper of 600, 800, and 1200 grit sizes on an eight-inch grinding wheel spinning at 200 RPM for 10 min at each step. An optical microscope was used to verify removal of deformation at each step. Polishing was then performed using 3 μm, 1 μm, and 0.25 μm polycrystalline diamond media suspension on polishing cloth for 15 min. Between each step of grinding and polishing the sample was sufficiently cleaned using DI water and soap to remove previous polishing media. After the final polishing step, cleaning with DI water and a clean fluffed Q-tip was performed to remove any excess residue. SPM imaging of each sample revealed an average roughness below 5 nm, and the indentation depth of the hardest sample (lowest depth) exceeded 75 nm. To obtain statistical results, 20 indents were performed on the cross-section of individual machining chips and three chips were tested to collect 60 data points in total. For powder samples, 10 indents were performed on the cross section of individual powder particles and ten particles were tested for each type of powder. Therefore, 100 data points were obtained for each type of powder. For single tracks, 60 indents in total were performed on the cross sections of individual samples.

Chapter 3 Evolution of Powder Morphology and Particle Size

A theoretical analysis is performed to investigate the impact force on powder during milling, and the consequent maximum deformation depth during milling was found to influence particle size refinement and morphology. The modeling results are used to identify a ball milling procedure that efficiently reduces particle size and forms near-spherical morphology in powders created from recycled machining waste. A dual-stage milling approach is implemented to verify the effect of ball diameter on the morphology and particle size. The powders fabricated from the dual-stage milling approach are more spherical than the powders created from the single-stage milling, and a greater fraction of powder (69 wt.%) is within 38-150μm, a particle size range of interest for laser engineered net shaping (LENS®). Other ball milling procedures were performed in liquid nitrogen, argon, and ethanol using various stainless steel feedstock. The results of these milling procedures support the modeling results and confirm the selected parameters used to produce alternative metal AM feedstock.

3.1 Impact Theory in Planetary Ball Milling

To understand the correlation between ball milling parameters and powder properties, both the force per impact and impact stresses are evaluated for different ball diameters. The stress per impact determines a maximum deformation depth in the powder particle, which subsequently determines the final morphology and particle size of the powder. A change in ball size influences the maximum deformation depth when the total energy transfer rate is maintained. Consequently, the particle size and the morphology of

41

powders are manipulated. The following sections provide theoretical analysis of the stress per impact and the maximum deformation depth per impact. The modeling results are used to guide the selection of ball diameters in planetary ball mill to convert machining chips to powders with particles size and morphology suitable for using in metal AM.

3.1.1 Stress per Impact

The morphology evolution from chips to powders significantly depends on the impact forces between the chips/powders and the milling balls [2,45,47–49]. The force per impact that a ball exerts on a particle can be quantified using both the milling parameters and the planetary mill dimensions (Figure 3.1). The maximum force per collision between balls results in stresses on the powder, which subsequently lead to plastic deformation of the powders and alter the morphology and particle size of the chips or powders that are ball milled. While the ball to powder weight ratio determines the overall energy that transfers from the milling balls to the powder, ball diameter is a critical milling parameter that influences the force per impact, the stress per impact, and the impact frequency. Previous studies have reported various morphologies (e.g., flakey or rock-like) and particle sizes for ball milled powders when the ball milling parameters are varied [36,39,41,42,98]. However, few studies performed quantitative analysis on how the selection of ball diameter affects the ultimate shape and particle size of the powder.
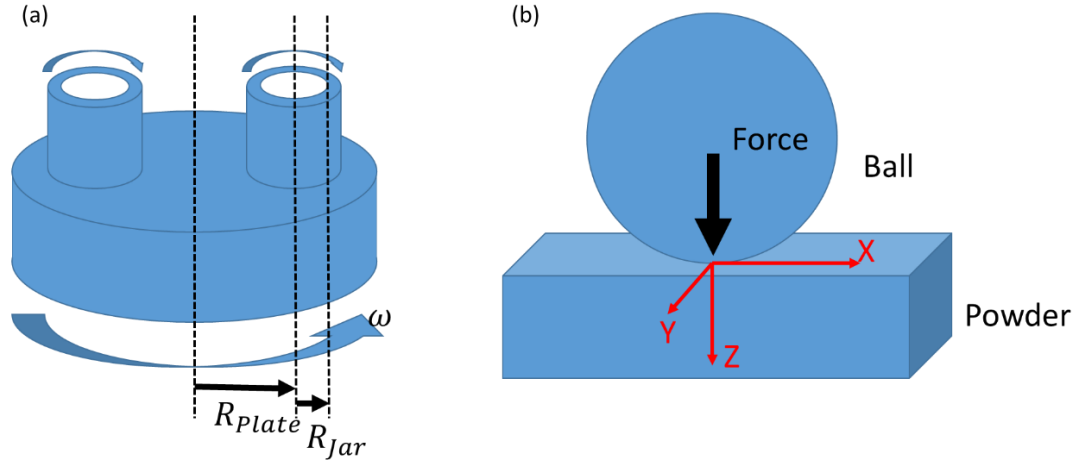
Figure 3.1: (a) Schematic diagram of the planetary ball milling setup; (b) Schematic diagram showing the impact between the milling ball and the powder/machining chips.

In an effort to select appropriate ball milling parameters to create near-spherical powders with particle sizes of 38-150 μm, the desirable powder characteristics for LENS®, Gusev's model and Hertz's model [50,99] are combined in the current study to evaluate the impact force and stress on the powder, as well as the resultant maximum deformation depth in the powder. Two different types of balls are used as the milling media: Φ-20 balls and Φ-6 balls. Gusev et al. developed a model that calculate the maximum force per collision in a planetary ball mill relative to the position in the ball mill as follows [50]:

$$F(t) = ma(t) \qquad \qquad \textbf{Equation 3.1}$$

$$a(t) = \left[\left(\frac{d^2 x}{dt^2} \right)^2 + \left(\frac{d^2 y}{dt^2} \right)^2 \right] \qquad \qquad \textbf{Equation 3.2}$$

$$a(t) = 4\pi^2 \omega^2 \left(R_{Plate}^2 + R_{Jar}^2 + 2R_{Plate} R_{Jar} Cos[4\pi\omega t] \right)^{\frac{1}{2}} \qquad \textbf{Equation 3.3}$$

where m is the mass of the ball, a is the acceleration rate, t is time, x and y define the position relative to the center axis of the mill, ω is the angular speed of rotation, R_{Plate} is the radius of the main disk, and R_{Jar} is the internal radius of the jar. According to Gusev's model, the impact force increases as the ball approaches the furthest distance from the center axis. The

43

maximum force per impact from Φ-20 balls is 37 times greater than that from Φ-6 balls, as shown in Figure 3.2.
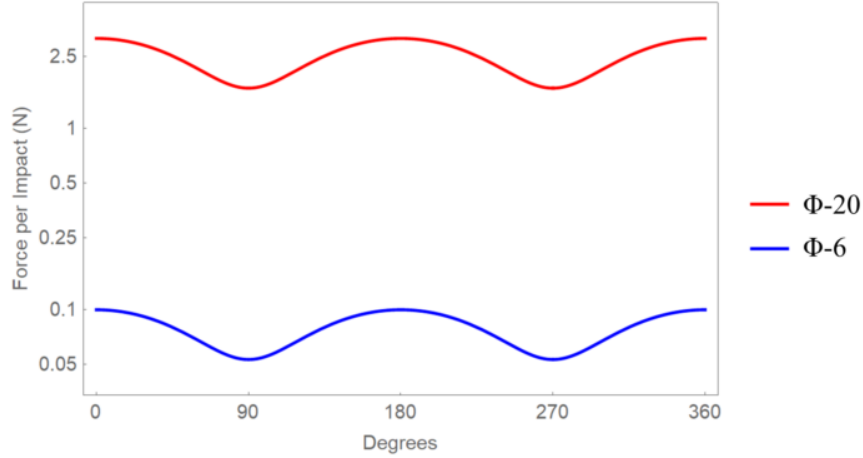
Figure 3.2: Maximum force per impact of Φ-20 and Φ-6 balls as a function of the turn angle in a PQ-N04 planetary mill.

Another model developed by Hertz [99] defines the maximum pressure (P_{max}) per impact between two spheres as a function of force and impact area (A) as follows:

$$P_{max} = \frac{3F(t)}{2\pi A^2}$$ **Equation 3.4**

where pressure varies as a function of lateral distance (X) from the center of impact [99]:

$$P(X) = P_{max}\sqrt{1-\frac{X^2}{A^2}}$$ **Equation 3.5**

The impact area (A) is a function of the impact force and material properties, as given in Eq. (6) below [99].

$$A = \sqrt[3]{\frac{3F(t)}{8}\frac{\left(1-v_{ball}^2\right)/E_{ball}+\left(1-v_{powder}^2\right)/E_{powder}}{\frac{1}{D_{ball}}+\frac{1}{D_{powder}}}}$$ **Equation 3.6**

where v is the Poisson's ratio, E is the elastic modulus, and D_{ball} and D_{powder} are the diameters of the colliding ball and powder, respectively. The stress at any distance from the center of impact is defined as [99]:

$$\sigma_x = \sigma_y = -P(X)\left[\left(1-\left|\frac{Z}{A}\right|\tan^{-1}\frac{1}{|Z/A|}\right)(1+\nu)-\frac{1}{2\left(1+\frac{Z^2}{A^2}\right)}\right]$$

Equation 3.7

$$\sigma_z = \frac{-P(X)}{1+\frac{Z^2}{A^2}}$$

Equation 3.8

$$\sigma_V = |\sigma_x - \sigma_z|$$

Equation 3.9

where σ_V is the simplified von Mises stress and Z is the distance from impact into the particle, as shown in Figure 3.1b.

Coupling Gusev's model of maximum impact force [50] with Hertzian stress approximations [99], a correlation between the ball diameter and the maximum stress in a powder particle is elucidated. Comparison between the impact stresses and the strength of the feedstock provides guidance to identify proper milling parameters for preferred morphology and particle size reduction. To determine the starting parameters, deformation imparted on the feedstock by different ball diameters are discussed in next section.

3.1.2 Effect of Parameter Manipulation

To study the influence of various ball diameters on powder morphology evolution, the maximum deformation depth per impact is determined by applying the milling parameters outlined in the experimental procedure to identify the Z depth at which the von Mises stress, σ_V, is equal to the yield strength (YS) of 304L (210 MPa [100]). Only the direct collision between a ball and a particle is considered in the model, as the stress resulting from the self-rotation of the balls and the powder particles is negligible when compared to the direct impact stress. The milling model suggests, assuming a constant ball-to-powder ratio and the dimensions of the mill do not change, that the max deformation depth increases as RPM, ball diameter, and the elastic modulus of the balls increase.

An increase in the RPM will increase the ball velocity and increase the impact frequency, and vice versa. Changing the elastic modulus can be done by changing the materials of the balls. But this may introduce unwanted contamination. If the ball-to-powder weight ratio is constant, increasing the ball diameter will decrease the impact frequency and increase the total mass of the balls, which corresponds to an increase in max deformation depth. In addition, reducing the RPM of the mill with a constant ball-to-powder weight ratio will reduce the energy transfer rate from the balls to the powder, while changing the diameter or the elastic modulus of the balls does not affect this transfer rate. A high energy transfer rate is needed to convert the machining chips to powders with reduced particle size and near-spherical morphology in a relative short amount of milling time. Increasing the energy transfer rate can be achieved by either increasing the ball-to-powder weight ratio or using a high RPM. However, increasing the ball-to-powder weight ratio decreases the amount of the initial feedstock and thus reduces the yield of the final powder for a milling jar with fixed volume. On the other hand, increasing RPM changes how energy is transferred to the powder, i.e., changing the max deformation depth per impact. In contrast, decreasing the ball diameter decreases the max deformation depth and increases the frequency of impacts, while it does not change the yield of the final powder. Therefore, varying the ball size is an effective way to tailor the characteristics of powders during ball milling.

When the models are applied to the milling procedure outlined in CH2, the results suggest that the maximum deformation depth per impact from Φ-6 balls, Φ-10 balls, and Φ-20 balls, is approximately 13 μm, 28 μm, and 81 μm, respectively (Figure 3.3). This maximum deformation depth increases as the difference between feedstock particle size and ball size increases. For example, when the ball diameter is increased to two times of the previous one

(e.g., from 10 mm to 20 mm), each impact results in an increase of the maximum deformation depth to approximately three times of the previous value.
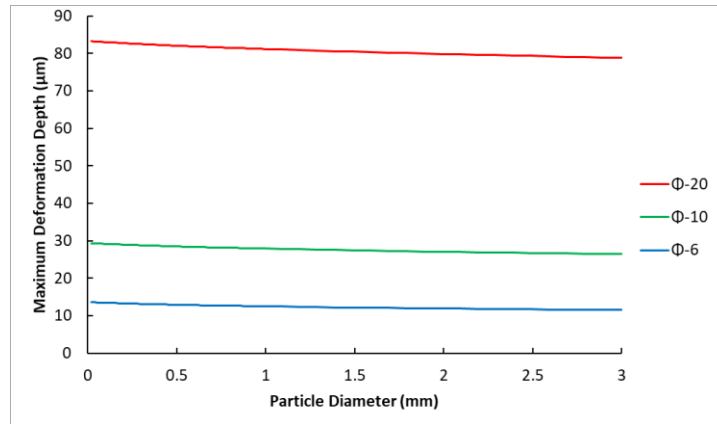
Figure 3.3: Maximum deformation depth of a particle impacted by Φ-20, Φ-10, and Φ-6 balls as a function of particle diameter.

When the maximum deformation depth is normalized by the particle diameter near the ideal particle size range for LENS® (38-150 μm), the dependency of ball diameter on final particle morphology is demonstrated in Figure 3.4. For example, the normalized maximum deformation depth in a 100-μm-diameter-particle caused by the impact from a Φ-20 ball is approximately 81% of the particle diameter; while that caused by the impact from a Φ-10 ball and from a Φ-6 ball is 28% and 12% of the particle diameter, respectively. This change in maximum deformation depth is supported by the experimental observation that will be discussed in Section 3.2.
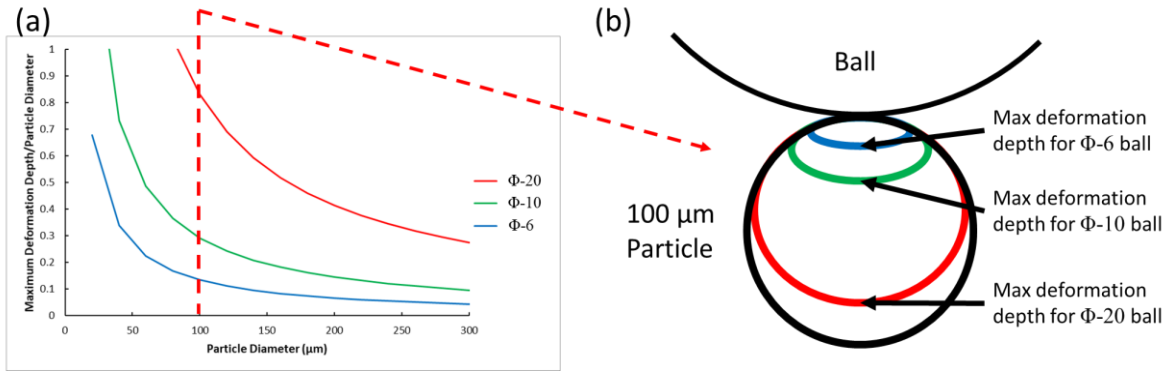
Figure 3.4: (a) Normalized maximum deformation depth of a particle impacted by Φ-20, Φ-10, and Φ-6 balls as a function of particle diameter. (b) Schematic representation of the maximum deformation depth induced on a 100 μm particle by the impact from Φ-20 (red line), Φ-10 (green line), and Φ-6 (blue line) balls.

If the ball-to-powder weight ratio is maintained, changing the ball diameter not only affects the force per impact but also the frequency of the impacts. With a consistent ball-to-powder weight ratio, when the ball diameter is increased to two times of the previous value (e.g., from Φ-6 to Φ-12), the impact frequency is decreased to 1/8 of the previous value, while the force per impact is increased to eight times of the previous value. In addition, each impact results in an increase of the maximum deformation depth to approximately three times of the previous value. This relationship between the normalized maximum deformation depth and ball diameter indicates using Φ-6 balls is more favorable for forming spherical morphology in the powders with particle sizes ranging from 38 μm to 150 μm, as a large deformation depth, particularly when it exceeds 50% of the particle diameter, tends to produce flakey or flattened powder. This speculation based on the modeling results is verified by experimental results provided in next section.

The maximum deformation depth is also associated with the yield strength of the materials that are ball milled, which may be increased during ball milling due to strain hardening, grain boundary strengthening, and phase transformation. Although the

theoretical model has limitations due to only accounting for direct impacts where all forces are transferred into one given particle, it provides fundamental insight into the role of ball diameter in the plastic deformation in a powder particle during ball milling.

3.2 Experimental Investigation of Powder Fabrication from Machining Chips

The powders that were fabricated from machining waste chips at different stages of the ball milling using different ball sizes were characterized in terms of particle size, morphology, and microstructure. These characteristics are important to determine the feasibility of use in metal AM. Several methods, such as SEM, XRD, and sieving were applied to study these characteristics. The effects of changing ball diameter, milling environment, and temperature are discussed.

3.2.1 Particle Size Evolution

Understanding of the particle size evolution during milling is a critical goal of this study. To use powder in LENS®, a small particle size distribution (38-150 μm) is preferred for enhanced flowability of the feedstock through the powder feeder, high printing resolution, and decreased porosity in the final parts [2,26,30]. The rate of reduction in particle size depends on the stresses induced on the feedstock during milling. In the present study, the maximum deformation depth was varied by changing the ball diameter.

The particle size distributions for the various ball milled powders are provided in Figure 3.5. The yield of the powder with particle sizes of 38-150 μm for BM-2Stg-Int-36hr, BM-2Stg-Int-48hr, and BM-2Stg-Int-60hr was approximately 21 wt.%, 37 wt.%, and 53 wt.% of the initial input, respectively. Increasing milling time with the Φ-6 balls increases the number fraction of powder particles with sizes of 38-150 μm. For the dual-stage ball milling

49

without interruption (BM-2Stg-60hr), the yield of powder with a particle size range from 38-150 μm is 69 wt.%. In contrast, BM-20-60hr and BM-6-60hr only yielded 2 wt.% and 3 wt.% of powder with a particle size of 38-150 μm, respectively. These results indicate that the dual-stage milling process is more effective in reducing the particle size to below 150 μm than either single stage process for an equivalent total milling time (60 hours).
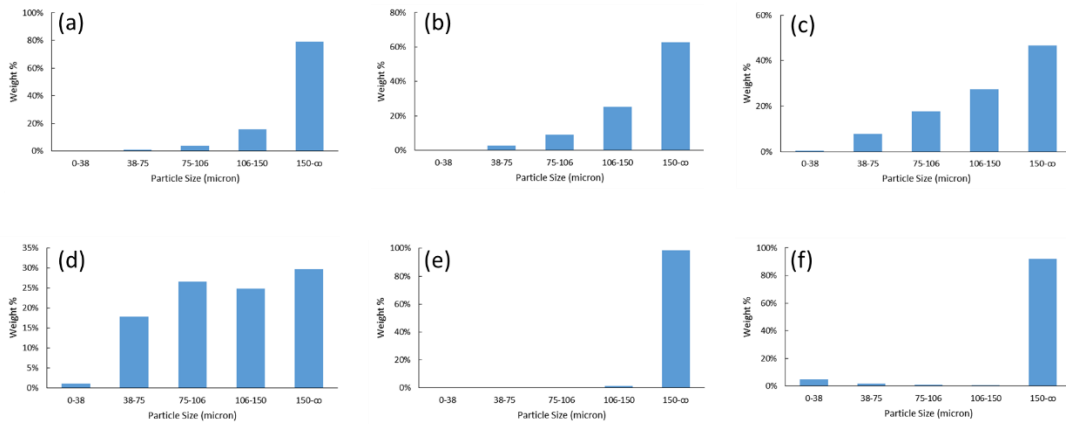
Figure 3.5: Particle size distributions in various ball milled powders from sieving: (a) BM-2Stg-Int-36hr, (b) BM-2Stg-Int-48hr, (c) BM-2Stg-Int-60hr, (d) BM-2Stg-60hr, (e) BM-20-60hr, and (f) BM-6-60hr.

A comparison between the result from the dual-stage milling approach and that from the single-stage milling method for equivalent milling time illustrates that the particle size refinement and morphology evolution of the powders observed experimentally are consistent with the prediction from the theoretical analysis of the maximum deformation depth. Both the modeling results and the experimental observation suggest particle size refinement is achieved by impacts with high forces. Particle size refinement occurs when a particle is cleaved into parts. This happens as a particle is either split by one large impact, or by the accumulation of multiple impacts that propagate a crack through the particle. To efficiently reduce the particle size, the modeling result reveals that the impact stresses need

to be sufficiently high to propagate cracks through a particle while not exceeding the critical value leading to cold welding.

To summarize, efficient refinement of 304L steel chips with a length scale of millimeters to powders with a scale of 38-150 μm by planetary milling requires a dual-stage approach. Using Φ-20 balls at the initial milling stage provides sufficient plastic deformation to break the coarse chips into sizes that the Φ-6 balls can refine. Once the chips have been refined to a length scale of several hundred microns, the Φ-6 balls break down the intermediate particles to form suitable morphology (near-spherical) and particle sizes for AM more efficiently than the Φ-20 balls, as the Φ-6 balls impact the powder more frequently, and the maximum deformation depth is significantly reduced. As a particle is impacted by a high frequency of low forces from random directions, the aspect ratio of the particle decreases.

3.2.2 Morphology Evolution

Table 3.1 provides quantitative information on the morphology evolution of BM-2Stg-Int-24hr, BM-2Stg-Int-36hr, BM-2Stg-Int-48hr, and BM-2Stg-Int-60hr powders, including the particle aspect ratio and the number percentage of the flattened particles in each type of the powder. The values were obtained by analyzing SEM images via ImageJ®. The closer the aspect ratio is to 1, the more spherical the powder is. 1% (number percentage) of the particles in BM-2Stg-60hr powder are classified as flattened, while the average aspect ratio is 1.37. In contrast, the BM-20-60hr powder contains 38% (number percentage) flattened particles.

Table 3.1: Comparison of the number percentage of flattened powder particles and the aspect ratio of the powder particles among the various powder samples.

Sample ID	Number Percentage of Flattened Particles	Aspect Ratio			
		Average	D30	D50	D80
BM-2Stg-Int-36hr	92%	1.80	1.22	1.45	2.66
BM-2Stg-Int-48hr	16%	1.55	1.34	1.44	1.77
BM-2Stg-Int-60hr	2%	1.41	1.18	1.36	1.56
BM-2Stg-60hr	1%	1.37	1.21	1.34	1.55
BM-20-60hr	38%	2.15	1.62	1.91	2.70
BM-6-60hr	1%	1.39	1.21	1.32	1.56

The morphology of the powder collected between sieves 100-140 mesh (nominally particle size 106-150 μm) is shown in Figure 3.6. GA powder is generally described as spherical powder with a smooth surface, compared to WA powder that exhibits relatively irregular morphology. BM-2Stg-60hr powders exhibited rounded features and smoother surfaces than the powders created from single-stage milling (Figure 3.6a-b). BM-20-60hr (Figure 3.6c-d) show flattened particles, and BM-6-60hr (Figure 3.6e-f) show near-spherical agglomerates with rough surfaces. The low number percentage of flattened particles combined with the smooth surface features observed in the BM-2Stg-60hr powder indicate a more ideal powder morphology for metal AM is achieved when using a dual-stage milling approach as opposed to the single-stage milling approaches of BM-20-60hr or BM-6-60hr. BM-2Stg-60hr powder exhibited a coarser surface than both GA and WA powders [2,11]. However, this powder exhibits a more spherical morphology when compared WA powder [2]. As discussed in the CH 1, the use of WA powder as feedstock for metal AM suggested the feasibility of using non-spherical powders, such as the ball milled powder generated from machining chips in the present work.
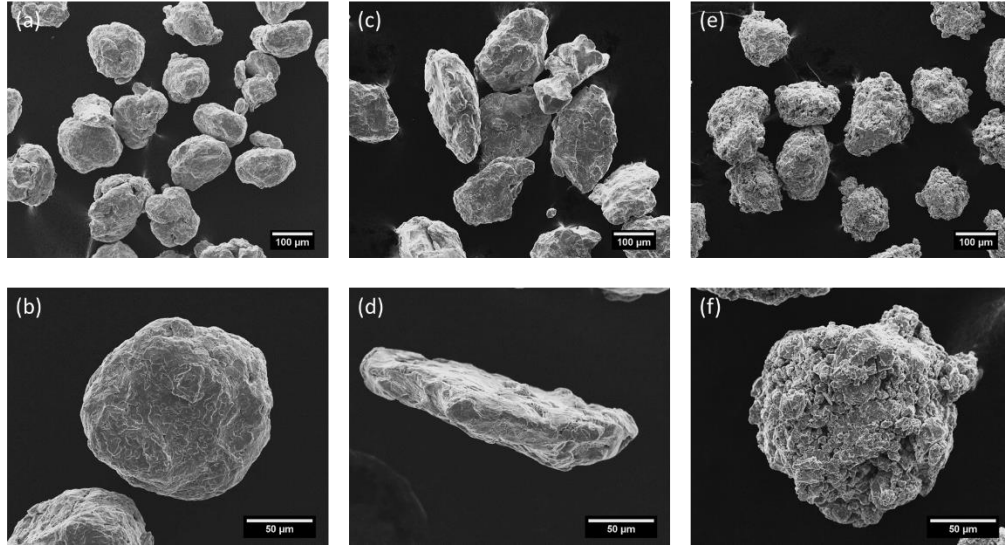
Figure 3.6: Representative SEM images of (a,b) BM-2Stg-60hr, (c,d) BM-20-60hr, and (e,f) BM-6-60hr powder between 100-140 sieves.

The evolution of morphology in the interrupted ball milling test is shown in Figure 3.7. Both the aspect ratio and the number percentage of flattened particles in BM-2Stg-Int powder decrease with increasing milling time. The morphology of the feedstock (BM-2Stg-Int-24hr) for stage two can be described as flattened rock-like particles with sizes ranged from 100-700 μm (Figure 3.7a). BM-2Stg-Int-36hr powder contains some particles with rounded features and smoother surfaces (Figure 3.7b); but 92% (number percentage) of the particles remained flattened. BM-2Stg-Int-48hr powder contains particles with spherical features such as increased thickness while maintaining the rounded features and smooth surfaces as is observed in BM-2Stg-Int-36hr (Figure 3.7c). However, 16% (number percentage) of the particles were still flattened. BM-2Stg-Int-60hr powder particles exhibit near-spherical features and smooth surfaces when compared to these from single-stage milling (Figure 3.7d), while only 2% (number percentage) of the particles remained flattened. Both the aspect ratio and the number percentage of flattened particles in the interrupted tests show a decreasing trend with increased milling time.
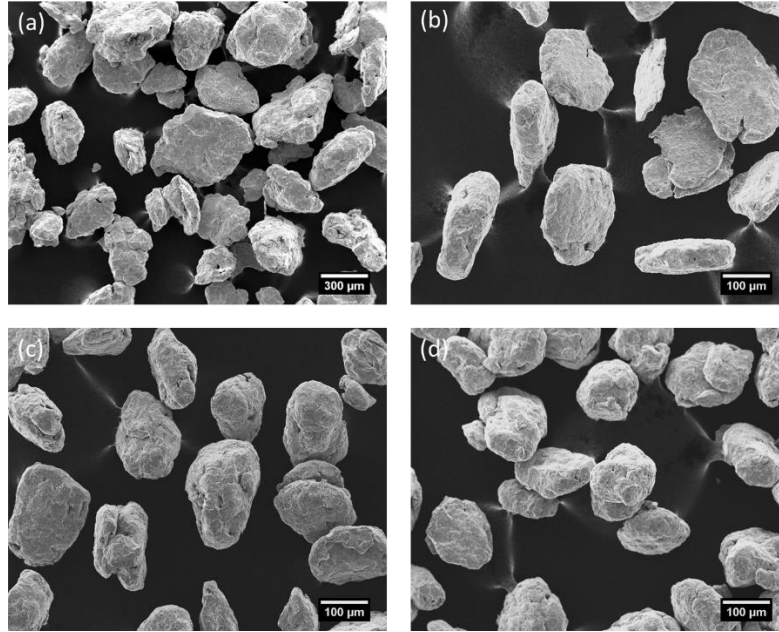
Figure 3.7: Representative SEM images of: (a) BM-2Stg-Int-24hr, (b) BM-2Stg-Int-36hr, (c) BM-2Stg-Int-48hr, and (d) BM-2Stg-Int-60hr powders, respectively.

As the particle is impacted by a high frequency of impacts with low maximum deformation depth from random directions, the aspect ratio decreases. Despite the inherent challenge of correlating 2-dimentional measurement to 3-dimensional morphology, the changing trend of the average aspect ratio values as a function of the ball diameter and the milling time indicates that milling with Φ-6 balls effectively modifies the powder morphology towards spherical.

In metal AM, a powder metallurgy consolidation technique of particular interest in current research, powder morphology is considered as one of the most critical characteristics of the feedstock [2]. The modeling work described in Section 3.1 provides useful insight into the effect of the milling ball diameter on the plastic deformation in a powder particle in the planetary ball mill. The experimental results suggest that a high frequency of low-force impacts on individual particles is preferable to form spherical or near-spherical morphology of the powder. As a particle is struck from multiple random

directions with low force impacts, it tends to form a spherical morphology. This is evidenced quantitatively by the decrease in aspect ratio and qualitatively by the increase in rounded features and smooth surfaces of the powders collected from the interrupted dual-stage milling.

3.2.3 Phase Identification

The X-ray diffraction (XRD) patterns of as machined 304L steel chips, GA powder, and BM-2Stg-60hr powder are shown in Figure 3.8. Both austenite and martensite are identified in the as machined 304L steel chips. The intensity of the austenite peaks was much greater than that of martensite. In BM-2Stg-60hr powder, the peaks corresponding to martensite were more intense than the austenite peaks. Plastic deformation induced phase transformation from metastable austenite to martensite has been observed in fatigued [83,85,101] and ball milled 304L steel [39]. 304L steels that were processed by forging and rolling at room temperature also consisted of dominant metastable austenite with some martensite [102]. As a bulk part is machined, the 304L steel chips experience plastic deformation, leading to an increase in the volume fraction of martensite. Severe plastic deformation during ball milling also induces the austenite to martensite phase transformation.
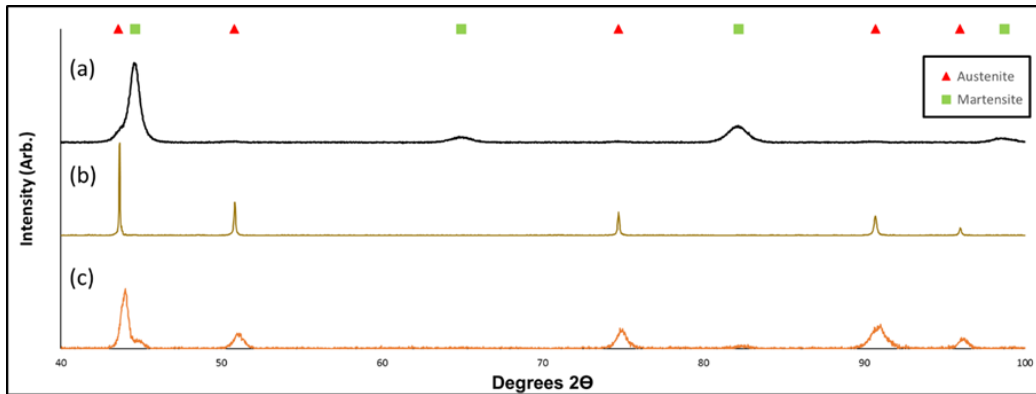
Figure 3.8: X-ray diffraction patterns of: (a) BM-2Stg-60hr powder, (b) GA powder, and (c) as received chips.

The XRD patterns showed that the 304L machining chips consist of a primary austenitic phase and a small amount of martensite. After the ball milling, the primary austenitic phase transforms to the martensitic phase in the ball milled powder, as illustrated by the higher intensity of the peaks corresponding to martensite than that for the austenite. The phase change is induced by the repeated impact of the balls on the powder at room temperature [39,84]. The modeling results show that the yield strength of the steel is surpassed with each impact. Thus, plastic deformation occurs in the powder. During ball milling, the dislocation density in the powder increases due to the plastic deformation. As the ball milling time increases, the dislocations rearrange themselves through pile-up and annihilation to form subgrain boundaries, which finally transform to high angle grain boundaries, leading to grain size refinement [40,45,50,52,77]. The combination of martensite formation and grain size reduction is expected to increase the hardness of the powder. As the hardness and strength of the powder increase during the ball milling, the powder exhibits increasing resistance to plastic deformation [99]. Consequently, a near-spherical morphology is achieved by the increased frequency of low-force impacts from the Φ-6 balls. Powder with a near-spherical rock-like morphology was successfully created from

56

recycled machining chips by implementing a novel dual-stage mechanical milling approach. The milled powders have been characterized by SEM, XRD, and sieving. Particle size refinement and morphology evolution in a ball mill agrees with the theoretical analysis in the present work. While the Φ-20 ball size is sufficiently large to break down the 5-20 mm chips to <150 μm given adequate ball milling time, the implementation of Φ-6 balls increases the frequency of low-force impacts, which refines the powder with particle sizes of 500-1000 μm to fine particles faster than the Φ-20 balls, with a more spherical morphology.

A phase change from metastable austenite to martensite was realized in the ball milled powder. This phase change is difficult to attain without the use of severe plastic deformation techniques. This phase change along with other common strengthening mechanisms that occur during ball milling, such as grain size refinement and increased dislocation density, are expected to increase the yield strength of the material [40–42,52,63,70]. This increase in yield strength during milling facilitates the formation of a spherical morphology by decreasing the maximum deformation depth. Because of the differences in yield strength associated with material, ball milling parameters, and starting feedstock size, further work is required to identify and predict the yield strength and determine the ideal parameters for preferred morphology formation.

3.3 Other Types of Ball Milling

Additional ball milling studies were performed to verify the validity of the ball milling theory and to identify the effect of other ball milling parameters that were not accounted for in previous sections. Ball milling of GA 316L and thick waste chips in ethanol or in argon was investigated, as well as the cryomilling method. By the manipulation of temperature,

feedstock size, and process control agents (PCAs), various final morphology and particle size were observed.

YS, temperature regulation, and PCAs influence the final morphology of ball milled 304L powders. An increase in yield strength is expected to decrease the maximum deformation depth per impact, while the effects of temperature and PCAs are more complicated. Ball milling at cryogenic temperatures is known to increase dislocation density and reduce grain size of crystalline materials at an accelerated rate when compared to ball milling at room temperature [40,41,77]. Further work is needed to determine the deformation induced by milling at cryogenic temperatures. Several PCAs and their effect on ball milling stainless steel have been studied previously [36]. It was found that duplex composition stainless steel powder milled in ethanol with addition of stearic acid formed a more flakey geometry than the powder that was milled without stearic acid. The following sections aimed to investigate the effects of ball milling parameters and powder properties in each of the aforementioned ball milling techniques on the powder morphology evolution.

3.3.1 Cryomilling of Stainless Steel

Cryomilling of metal powder often leads to a rocklike or flakey morphology depending on the milling parameters after 8 hours [40]. However, Cryomilling of both 304L thick waste chips and 316L GA powder yielded minimal morphological or particle size change in the initial feedstock. The cryomilled GA powder morphology (Figure 3.9) after 8 hours of milling with Φ-6 balls can be described as smooth and spherical with small dents on the surface, indicative of impact with the balls. This indicates that the milling stresses were not sufficient to refine the particle size, the frequency of high-velocity impacts was

58

insufficient to refine the feedstock, or the minimum particle size was coincidence with the size of the initial feedstock.
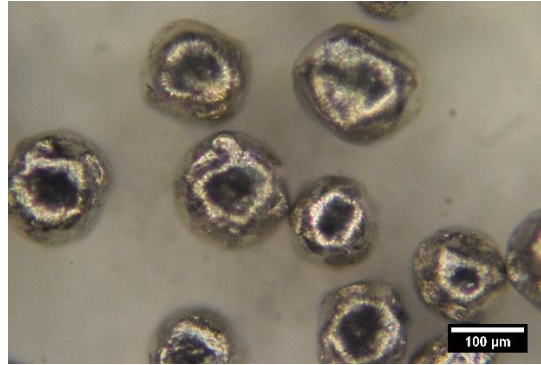
Figure 3.9: Representative optical images of cryomilled 316L stainless steel after 8 hours.

XRD of GA and cryomilled 316L powder shown in Figure 3.10 indicates that minimal transformation from austenite to martensite occurred when compared to what was observed in planetary ball milling of stainless steel. This supports the claim that either the milling stresses or the frequency of high velocity impacts were insufficient to refine this powder. If the powder had reached steady-state particle size, the fraction of martensite present is expected to be greater than the fraction of austenite [39,98]. Therefore, increased milling time with the same milling parameters, increased balls diameter, or increased RPM is recommended to refine the particle size and decrease the grain size of this powder.
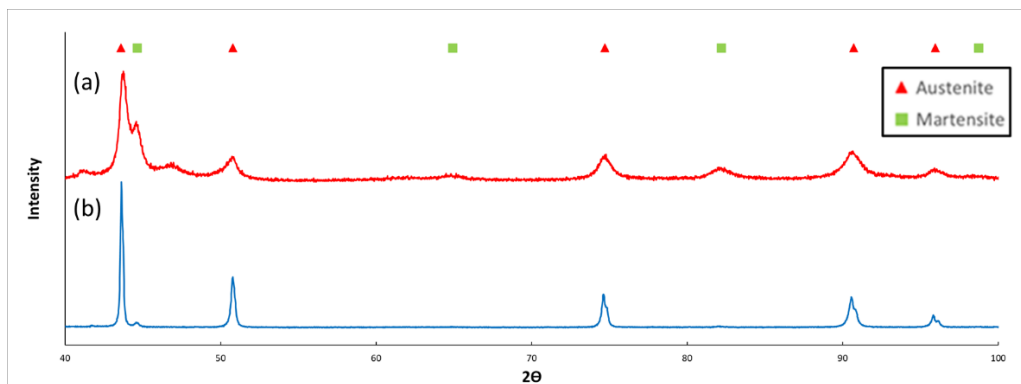
Figure 3.10: XRD pattern of (a) cryomilled 316L stainless steel, and (b) GA 316L stainless steel.

The morphology of the 304L thick chips remained unchanged after 8 hours of cryomilling (Figure 3.11). These thick chips differed from the machining chips used in the planetary ball milling study in Section 3.2 by a lack of serrations along the length and a slightly thicker cross section (~3-4 mm). The large initial particle size of the thick chips inhibited the Φ-20 balls from exerting the required stresses to refine the particle size. However, after the first 4 hours of cryomilling, XRD patterns reveal a significant portion of the chip surface transform from austenite to martensite (Figure 3.12). This transformation indicates the Φ-20 balls did provide sufficient stresses to deform the surface of the chips, Nevertheless, the lack of particle size reduction indicates that the maximum deformation depth is not large enough to reduce the particle size efficiently. To refine these chips via ball milling, it is recommended to increase the balls diameter, increase the RPM, or continue milling for significantly long time.
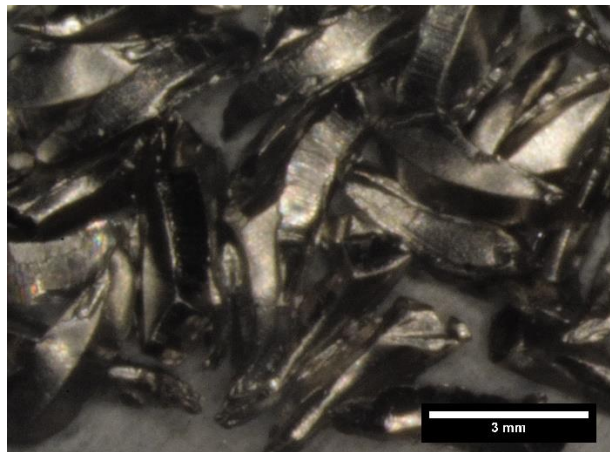
Figure 3.11: A representative optical image of the thick chips after cryomilling for 8 hours.
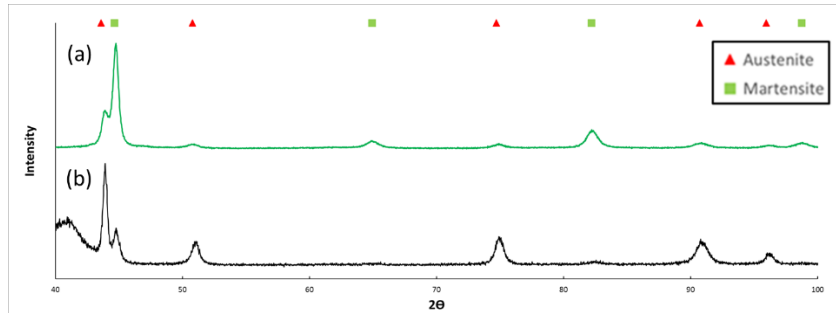
Figure 3.12: XRD pattern of (a) cryomilled thick chips, and (b) as received thick chips.

3.3.2 Planetary Ball Milling of GA 316L

Planetary Ball milling of GA 316L powder feedstock in both argon and ethanol was performed to identify the effects of high-impact stresses on powder that has not been plastically deformed. Ball milling of GA powder with Φ-20 balls in argon yielded no powder after 12 hours due to cold welding of the feedstock to the balls, as shown in Figure 3.13. The cold welding of the powder feedstock to the milling balls is attributed to the lower yield strength of the GA powder. The GA powder is expected to have a lower yield strength than the powder that has been ball milled for more than 24 hours. The low yield strength combined with high-impact stresses caused by milling with Φ-20 balls resulted in the cold welding of the powder to the balls and walls of the jar. This agrees with the impact theory for ball milling discussed in Section 3.1.2, as the maximum deformation depth of the Φ-20 balls on the feedstock particle sizes (38-150 μm) is between 53 and 100% of the particle diameter. Furthermore, the yield strength used to determine the maximum deformation depth is more accurate for the GA powders than the powders made from milled chips. This is due to the lack of phase transformation, strain hardening, and grain boundary strengthening in the GA powders when compared to the powders made from machining chips via ball milling.

61
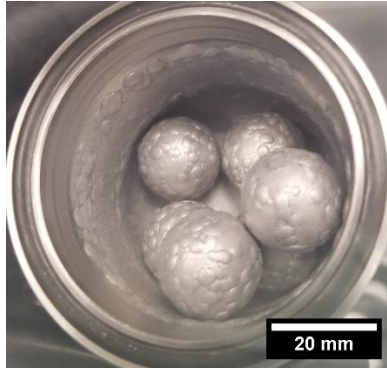
Figure 3.13: Particle welding of planetary ball milled GA 304L after 12 hours.

Ball milling of GA powder in ethanol with Φ-6 balls yielded flakey powder with a wide range of particle sizes after 12-hour milling time (Figure 3.14). The GA powder is expected to have a reduced yield strength when compared to the powder created from waste chips as it does not have deformation induced martensite, increased dislocation density, or reduced grain size that results from long milling times. This reduction in yield strength may have facilitated the flattened morphology. However, the ethanol did prevent cold welding of the chips to the balls and containers. Reduction of cold welding often leads to a smaller particle size distribution as well as flattened morphology. As shown previously in 3.2.2

Morphology Evolution, the Φ-6 balls impart enough deformation on the powder that small powder particles may agglomerate and cold melt to form a near-spherical morphology.
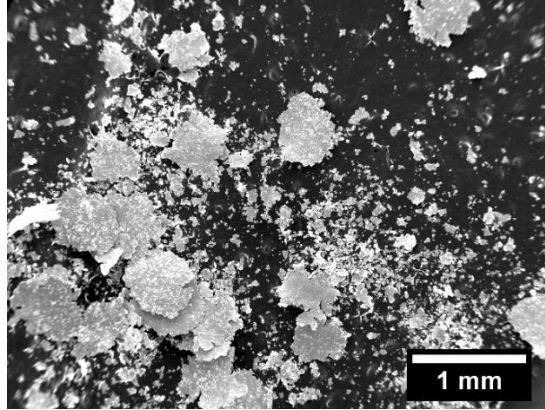
Figure 3.14: Representative SEM images of GA 316L powder milled in ethanol after 12 hours.

3.3.3 Planetary Ball Milling of Thick Chips

It took a significantly longer time to reduce the particle size of the thick chips ball milled in ethanol and argon with Φ-20 balls. This may be due to lack of serrations in this feedstock and a uniform thickness of the thick chips. After 96-hour milling, most of the thick chips remained larger than 1 mm. However, the morphology has become flattened as shown in Figure 3.15. To observe the differences between morphology evolution at room temperature in argon and ethanol, the remainder of the feedstock was milled by Φ-6 balls for 36 hours. After a total dual-stage milling time of 132 hours, approximately 87 wt.% and 67 wt.% of the thick chips milled in ethanol and argon remained coarse with a size above 150 μm, respectively.
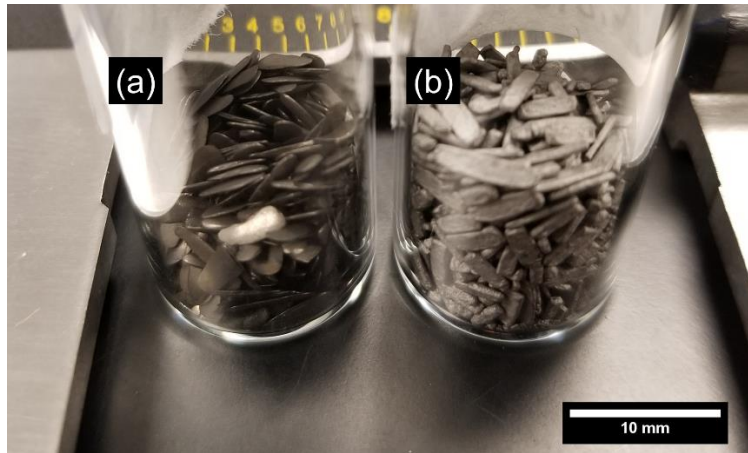
Figure 3.15: Representative image of flattened thick machined chips milled in (a) ethanol and (b) argon after 132 hours.

Figure 3.16 shows the morphology of the powder with size below 150 μm created from ball milling of thick machining chips. The morphology of the powder milled in ethanol can be described as fine and flakey (Figure 3.16a), and the morphology of the powder milled in argon can be described as near-spherical (Figure 3.16b). The differences in the powder morphology observed when milling in ethanol as opposed to milling in argon may be attributed to the suppression of cold welding. The thick machined chips milled in argon appear to consist of multiple small particles that have been cold welded together and smoothed by the repeated impact with Φ-6 balls. This is supported by the milling model as Φ-6 balls result in a max deformation depth of 13 μm. This suggests that the cold welding of the small particles is needed to form a more spherical morphology. In contrast, the small particle sizes found in the powder milled in ethanol suggest that the particle size can be reduced if only limited cold welding occurs.
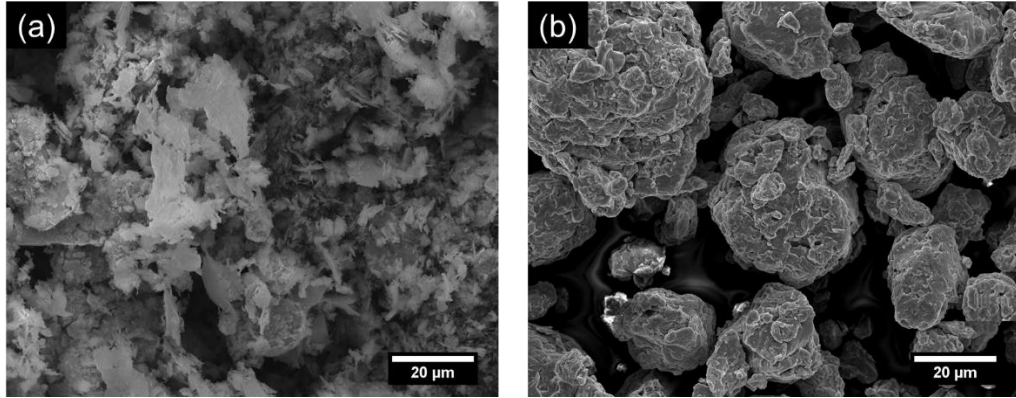
Figure 3.16: Representative images of powder made from thick machined chips milled in (a) ethanol and (b) argon after 132 hours.

Various ball milling strategies were performed to validate modeling results derived from the Hertzian impact stresses and to investigate the effect of ball diameter on the morphology evolution of the powder that are ball milled. Powders with near-spherical morphology have been successfully fabricated by ball milling of different stainless steel feedstock: including thin and long machining chips, as well as thick and short machining chips. The modeling results of the impact stress and maximum deformation depth in powder agree well with experimental observations.

Chapter 4   Use of Ball Milled Powder in Metal AM

To verify the feasibility of using the powder made from metal machining waste in metal AM, single tracks were deposited using a modified LENS® technique. Single tracks made from GA powder, denoted as ST-GA, were deposited using identical processing conditions for comparison purpose. Both types of single tracks were characterized in terms of continuity, porosity, melt pool geometry, grain structure, and chemical composition. The relevant results are compared and discussed in this chapter. In addition, the hardness of the machining chips, the GA powder, the ball milled powder fabricated from machining chips, and the single tracks are discussed in this chapter to investigate the feedstock-processing-property correlation.

4.1   Deposition of Single Tracks

Deposition of single tracks is commonly used to identify ideal processing parameters for different materials in metal AM before a large volume of bulk sample is fabricated [9,86–88]. Deposition of single tracks allows researchers to test multiple parameters with a limited volume of powder. Single tracks are often characterized by their continuity, melt pool geometry, porosity, the amount of spatter they produce, grain structure, and chemical composition [29,89–91,103]. Continuity and the amount of spatter can be characterized by optical microscopy of the surface of the single tracks, whereas melt pool geometry and porosity require imaging of the cross section of the single tracks. The grain structure and chemical composition are characterized by SEM combined with EBSD and EDS.

The grain structure of the single tracks is of interest because it has been shown that metal AM parts may exhibit anisotropic behavior [94,104]. Both morphological and textural

anisotropy of grain growth contribute to the differences in properties [93,94]. Morphological anisotropy is exhibited by elongated grains regardless of lattice orientation; whereas textural anisotropy is caused by preferred lattice orientation of grains [94]. In this section, the effect of processing parameters on the continuity, porosity, melt pool geometry, grain structure, and chemical composition of the single tracks is investigated.

4.1.1 Stability

Variance of deposition parameters can create single tracks with either stable or unstable melt pools. Single tracks with unstable melt pools are identified by discontinuous melting, bead-up, and porosity induced by vaporization of the metal [88,89]. Discontinuous melting and bead up of single tracks indicates the energy density should be increased, and vaporization induced porosity indicates the energy density should be decreased [87,88,90]. As shown in Figure 4.1, the single tracks made from the ball milled powder, denoted as ST-BM in the following section, show continuous melting for all three different deposition conditions. This indicates the laser power and the scanning speeds are sufficiently high to achieve stability in the ST-BM. ST-GA show similar continuity and stability at all processing parameters.
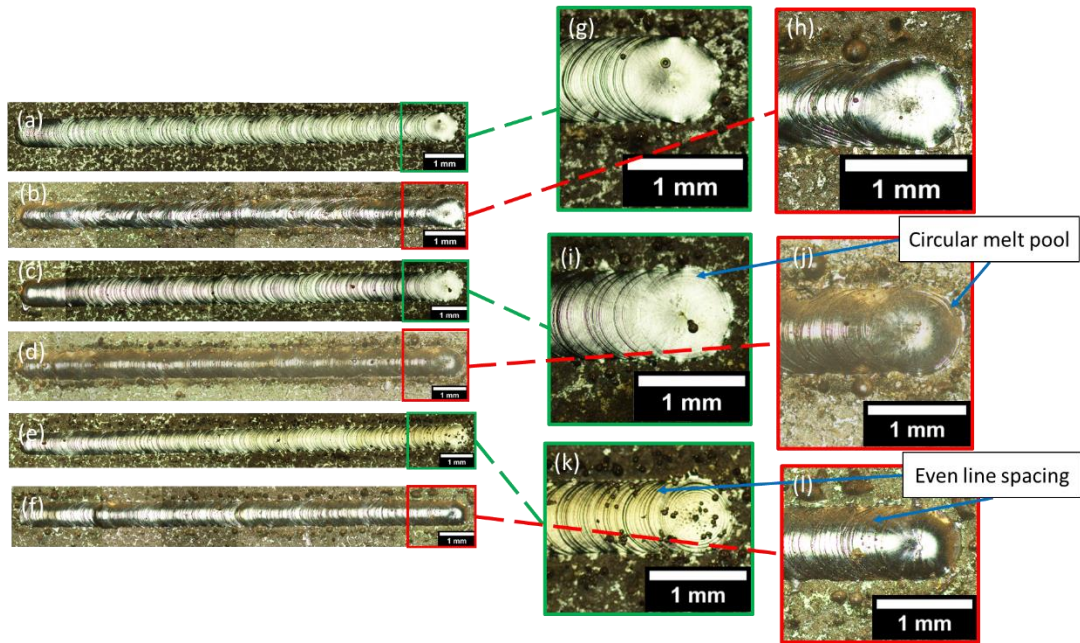
Figure 4.1: Optical images of (a,g) ST-GA-460-40, (b,h) ST-BM-460-40, (c,i) ST-GA-410-40, (d,j) ST-BM-410-40, (e,k) ST-GA-360-40, and (f,l) ST-BM-360-40.

Melt pool geometry and cooling line spacing also help to identify effective processing parameters. Even though line spacing and a circular melt pool are indicative of sufficient cooling time, the shape of the melt pool and solidification rate are influenced by the substrate material, while the grain growth is directly affected by the solidification rate and shape of the melt pool [91]. Optical images of single tracks shows that ST-GA-360-40 and ST-GA-410-40 have circular melt pools, ST-GA-460-40, ST-BM-410-40, and ST-BM-360-40 have elliptical melt pools, and ST-BM-460-40 has a final melt pool geometry between elliptical and tear-drop.

The melt pool geometry of ST-BM indicated that hotter melt pools formed during deposition of ST-BM as compared to ST-GA. To produce a more circular melt pool, a faster solidification rate or lower energy density should be used to deposit ST-BM [29,91]. The trailing edge of the melt pool lengthens as the scanning speed increases due to the time it

68

takes to solidify the molten metal [91]. In contrast, decreasing the laser power will decrease the energy that must dissipate to facilitate solidification [2].

The width of the single track often varies with laser power [2,91]. Single track width is also influenced by the laser spot size and melt pool geometry [91]. Figure 4.2 showed the average width of the single tracks deposited with different conditions. The average width of ST-BM-360-40, ST-BM-410-40, and ST-BM-460-40 are 718±20 μm, 809±24 μm, and 849±23 μm, respectively. In comparison, the average width of ST-GA-360-40, ST-GA-410-40, and ST-GA-460-40 are 688±19 μm, 780±24 μm, and 900±17 μm respectively. Both ST-BM and ST-GA show an increasing trend in average width with increased laser power.
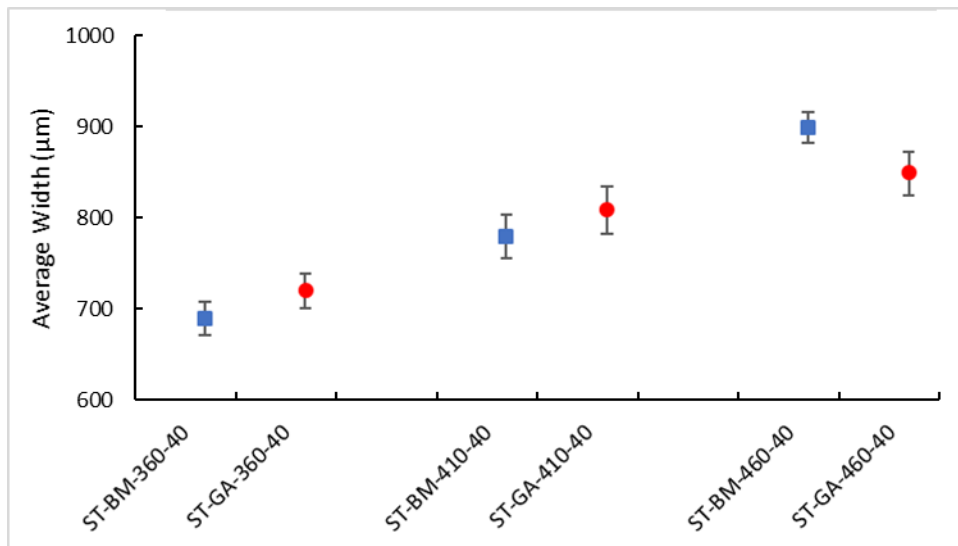
Figure 4.2: Average width of (red) ST-BM and (blue) ST-GA.

While the melt pool can often be manipulated by the deposition parameters, the primary mechanisms for solidification and grain growth will be determined by the substrate material and the feedstock powder [105]. In addition, the complex interaction between the substrate, melt pool, and powder during solidification cannot be identified solely from the

69

melt pool geometry and surface characterization. Cross-sectional microstructure was examined and discussed in the following sections.

4.1.2 Porosity

Pores in single tracks are attributed to several factors: the porosity in the substrate, the porosity in the feedstock powder, low packing density, insufficient shielding gas, or excessive heat in melt pools by vaporization of the substrate and powder [2,87,88,90]. As shown in Figure 4.3, limited porosity is found in both ST-GA and ST-BM. While several large pores above 3 µm were observed in both ST-BM and ST-GA, neither showed any trends in porosity content with changing laser power. All single tracks exhibited less than 4% (area percentage) porosity regardless of deposition parameters.
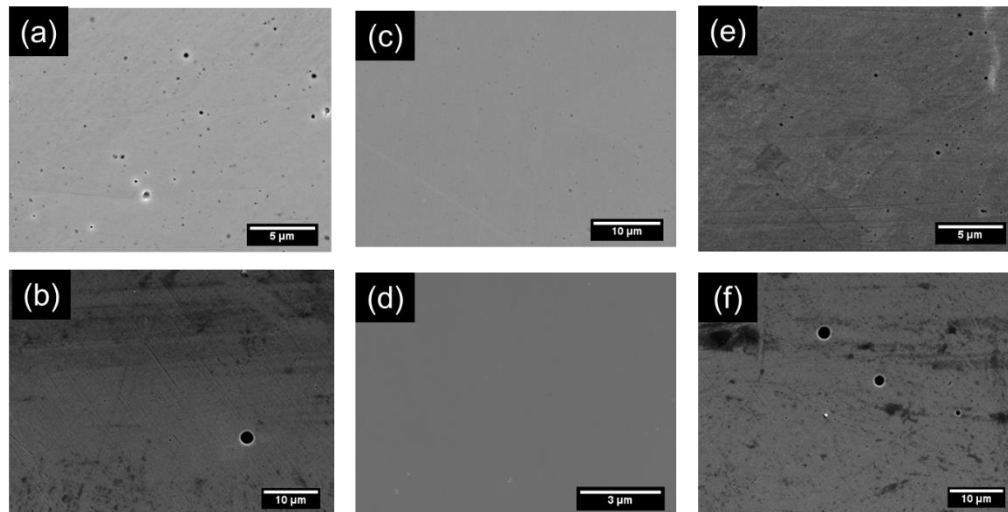
Figure 4.3: Representative SEM images of porosity in (a) ST-BM-360-40, (b) ST-GA-360-40, (c) ST-BM-410-40, (d) ST-GA-410-40, (e) ST-BM-460-40, (f) ST-GA-460-40.

Other studies have found pores in single tracks and bulk samples made from metal AM up to 70 µm [2,87,88,90]. However, these larger pores were observed in the single tracks made from high energy density, and many deposition conditions were tested [88,90,94]. In the single tracks made in this study no pores above 5 µm were observed.

4.1.3 Morphological and Textural Grain Anisotropy

The complex interaction between the substrate, melt pool, and powder during solidification within a single track lead to differences in grain growth. To characterize the effect of laser power on the anisotropy of grain growth, the cross-section microstructure of the single tracks was characterized by EBSD. Figure 4.4 illustrate the grain orientation maps of the various single tracks. As the laser power increases, both ST-BM and ST-GA exhibit more upright columnar grains along the cross sectioned surface of the melt pool. This is supported by the normalized average aspect ratio of the grains within the melt pool shown in Table 4.1.

.
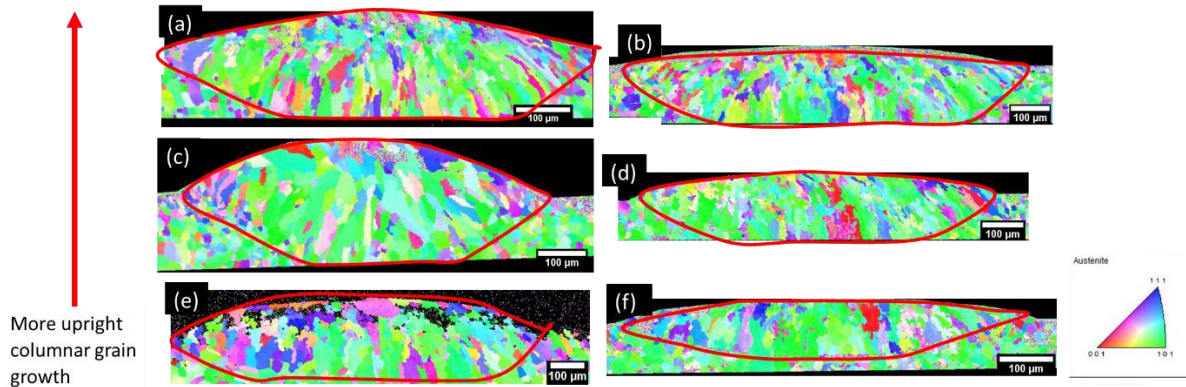
Figure 4.4: EBSD grain orientation maps of (a) ST-BM-460-40, (b) ST-GA-460-40, (c) ST-BM-410-40, (d) ST-GA-410-40, (e) ST-BM-360-40, and (f) ST-GA-360-40.

Table 4.1: Normalized Average Aspect Ratio of Grain

	Average Grain Aspect Ratio by area
ST-GA-360-40	2.88
ST-GA-410-40	3.31
ST-GA-460-40	3.06
ST-BM-360-40	2.85
ST-BM-410-40	3.07
ST-BM-460-40	3.46

The upright anisotropy of the grains is evidence of increased cooling time. When the melt pool solidifies quickly, the nucleation of many grains occurs simultaneously, and equiaxed grains are formed. However, hotter melt pools have slower cooling times which allows grains to grow in the direction of heat flow. These grains are also oriented towards the top melt as this region of the melt pool has the slowest cooling time due to the lack of conduction. It is also worth mentioning here that the geometry of the top of the ST-BM exhibit a progressively more prominent peak with higher laser power as shown in Figure 4.4. In contrast, the geometry of the top of the ST-GA are more flattened. The higher peak shown in ST-BM-460-40 is representative of a melt with a longer trailing edge or tear drop melt pool [91].

Both the ST-BM and ST-GA exhibited similar phase constitution, i.e., the area percentages of austenite and martensite do not differ between different single tracks. All single tracks consisted of less than 5 vol.% martensite. However, the confidence index for identification of martensite is low.

The grain orientation maps suggest that textural anisotropy is present in all single tracks. Preferred grain orientation occurs near to the (101) plane of austenite. Austenite

grains preferentially grow along the <100> direction [106]. The grains nucleate from the interface between the re-melted zone and the substrate, and grow at a bias towards the heat flow direction. The grains are also expected to grow at a bias towards the heat flow direction [29,93]. The prominence of this bias can be corelated to the deposition parameters [93]. High laser power combined with tear drop shaped melt pools often correspond to more columnar grain growth oriented to the face of the melt [91,93].

Both textural and morphological grain anisotropy were observed in the grain formation in the single tracks. The grain morphologies of ST-BM indicated that a higher laser power leads to more upright columnar grain growth. Anisotropy in grain structure lead to anisotropy in mechanical properties (e.g., strength and ductility) in the parts made by metal AM [94,104].

4.1.4 Grain Size Strengthening

Grain size significantly affects the strength of the material via the Hall Petch relationship [44]. The average grain size is determined using two methods. The first method uses the average volume of the grains to determine the diameter of a sphere of equivalent volume. The second method calculates grain size according to ASTM standard E112. Both methods excluded grains less than twice the step size (1.5 μm). Average diameter was found by equating the average volume to an assumed sphere. The average grain size of the various single tracks is summarized in Table 4.2. The average grain size of ST-BM and ST-GA are similar and show no dependency on the laser power. The similar grain size observed in ST-GA and ST-BM indicates that the solidification rates are also comparable [29].

Table 4.2: Average Grain Size of Single Tracks

	Average Grain Diameter in μm (number)	Average ASTM Grain Size in μm (number)
ST-BM-460-40	10.0	11.5
ST-GA-460-40	12.5	10.8
ST-BM-410-40	14.7	10.4
ST-GA-410-40	11.9	11.2
ST-BM-360-40	11.7	11.6
ST-GA-360-40	10.4	11.6

4.1.5 Chemical Composition

A representative EDS map of ST-BM-410-40 is provided in Figure 4.5 to show the chemical composition and the elemental distribution in the single track. The distribution of elements was homogeneous throughout the cross section of the single tracks. The in-homogeneity of chemical composition in stainless steel leads to anisotropic material properties.
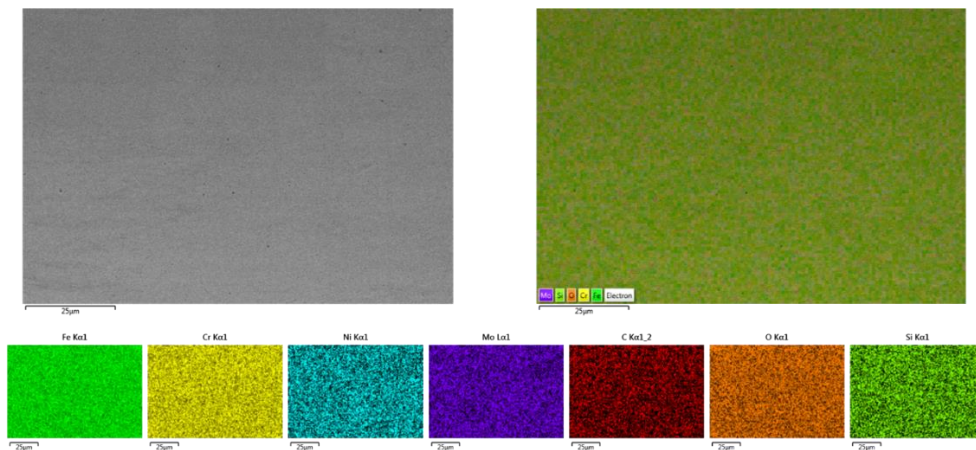
Figure 4.5: Representative (top-left) SEM image, (top-right) layered EDS element distribution map, and (bottom) individual elemental distribution maps of Fe, Cr, Ni, Mo, C, O, and Si.

EDS does not provide accurate quantitative information for light elements such as C and N [107]. Therefore, for the purposes of this study, the primary elements characterized were Fe, Cr, Ni, O, and Mo. Table 4.3 summarizes the wt.% of the elements found in ST-BM

and ST-GA. The average chromium, molybdenum, and oxygen contents of the ST-BM and ST-GA were approximately similar among the single tracks. The average nickel content in ST-GA is 9.7 wt.%, while the average nickel content in ST-BM is 8.0 wt.%.

Table 4.3: Elemental Composition (wt.%) of single tracks

	Fe	Cr	Ni	Mo	C	O	Si
ST-BM-460-40	68.7	17.7	8.3	1.4	2.9	0.5	0.5
ST-GA-460-40	67.2	17.6	9.8	1.4	3.1	0.5	0.5
ST-BM-410-40	69.5	17.7	7.7	1.1	2.9	0.6	0.5
ST-GA-410-40	67	17.6	10	1.6	2.7	0.6	0.5
ST-BM-360-40	69.3	17.7	7.9	1	3.1	0.5	0.5
ST-GA-360-40	67.2	17.6	9.4	1.7	3.2	0.5	0.5

While chromium and molybdenum content varied slightly between ST-BM and ST-GA, the major differences in composition between ST-GA and ST-BM is the nickel content: ST-GA has a higher nickel content of the ST-GA. Nominally 304L stainless steel contains between 8-12 wt.% nickel. The chemical composition of the machining chips, which was the starting material of this work, contained approximately 8.1 wt.% nickel. However, the Ni content of the GA 304L powder was not measured, but the EDS results suggest it was higher than that of the as-received chips that were milled into powder.

Increased nickel content in stainless steels deposited via metal AM changed the microstructure from equiaxed dendrite to columnar dendrite and decreased the hardness [9]. The difference of nickel content from 8.0 wt.% in ST-BM to 9.7 wt.% ST-GA may influence the mechanical properties of single tracks. Therefore, it is suggested to deposit single tracks with identical scanning parameters using a GA feedstock powder with a composition more indicative of the composition of the waste chips.

4.2   Nanoindentation

The hardness of GA powder, machined chips, and BM-2Stg-60hr powder was measured by nanoindentation. The local hardness of single tracks was also measured to determine if the hardness was dependent on the position in the melt pool and if there was a difference in hardness between ST-GA and ST-BM.

4.2.1 Powder

Figure 4.6 shows the differences in hardness between feedstock powder used in metal AM deposition and waste chips. The average hardness of the GA powder, machined chips, and milled powder was found to be 5.9 GPa, 6.4 GPa, and 9.2 GPa, respectively.
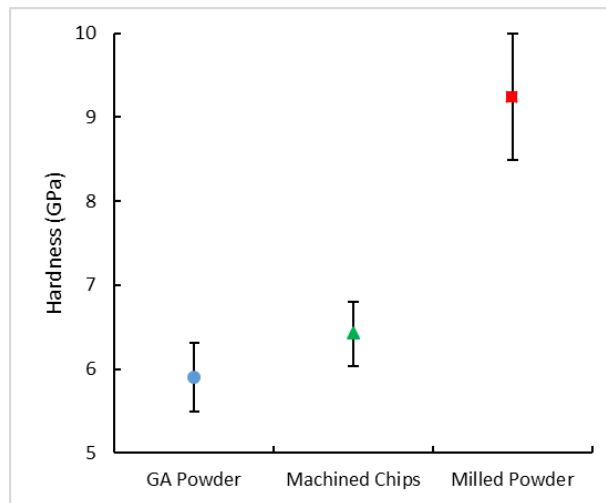
Figure 4.6: Nanoindentation hardness of (blue) GA powder, (green) machined chips, and (red) milled powder.

The nanoindentation hardness of the ball milled powder is 57% higher than that of the GA powder. The higher hardness of the BM powder is attributed to an austenite to martensite phase transformation [39,84], a reduction of grain size [41,42], and an increase in dislocation density [41,42] as discussed in CH 3. Machined chips also have a 9% higher

hardness than GA powder. This may be attributed to partial phase transformation induced by the plastic deformation of the machining operation [84].

The nanoindentation testing results suggest that the material is strengthened by the ball milling process. According to the modeling results, as the hardness and strength of the powder increase during the ball milling, the powder exhibits increasing resistance to further plastic deformation. Consequently, a near-spherical morphology is achieved by the increased frequency of low-force impacts from the Φ-6 balls. Testing the hardness of powder at various time intervals of ball milling could be used to account for changes in the maximum deformation depth calculation. This characterization may be used to determine parameters that are ideal for the formation of a spherical morphology in other complex material systems such as Al or Ti.

4.2.2 Hardness of Single Tracks

Initially indents with a max load of 1 mN were performed on ST-BM and ST-GA to maintain similar testing parameters between all hardness testing in this work. However, the size of pores present in the single tracks was near to the size indents. The max load was increased to 5 mN to diminish the effects of the pore size on hardness measurements. The hardness values relative to position in the melt pool were also characterized in both loading conditions.

4.2.2.1   1 mN Max Load

The average nanoindentation hardness of the single tracks (performed at a max load of 1 mN) is summarized in Figure 4.7. The hardness of ST-BM-360-40, ST-BM-410-40, and ST-BM-460-40 was found to be 4.4 GPa, 4.6 GPa, and 4.3 GPa, respectively. The hardness of ST-GA-360-40, ST-GA-410-40, and ST-GA-460-40 was found to be 4.0 GPa, 4.1 GPa, and 4.0

GPa, respectively. This corresponds to an average hardness in ST-GA and ST-BM of 4.0 GPa and 4.4 GPa, respectively.

Figure 4.7: Nanoindentation hardness of (red) ST-BM and (blue) ST-GA at 1 mN max load.

To determine the dependency of hardness on the indent position in the melt pool on, the indentation array was categorized according to x and y position. The x position corresponds to the horizontal direction of the cross sectioned single track, while the y position corresponds to the vertical direction. Figure 4.8 summarizes the dependency of nanoindentation hardness on x position, and Figure 4.9 summarizes the dependency of nanoindentation hardness on y position. No trends are observed between nanoindentation hardness and the position of the indent in the cross section of the melt pool.

Figure 4.8: Dependence of nanoindentation hardness on x position of (red) ST-BM and (blue) ST-GA at 1 mN max load.
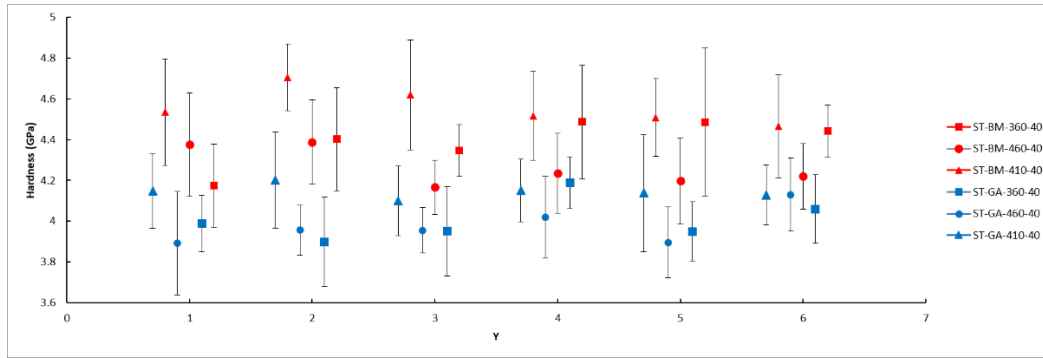
Figure 4.9: Dependence of nanoindentation hardness on y position of (red) ST-BM and (blue) ST-GA at 1 mN max load.

The lack of trends between position and nanoindentation hardness is justified by the EDS characterization which found a homogeneous distribution of elements all single tracks. The differences in hardness between ST-GA and ST-BM may be explained by the differences in Ni content found by EDS in Section 4.1.5.

Representative SEM images of the plastic deformation induced during nanoindentation of ST-BM (Figure 4.10a) and ST-GA (Figure 4.10b) indicate that size of the pores next to the indents cannot be neglected. To decrease the effects of the pores on indentation hardness the max load was increased to 5 mN.
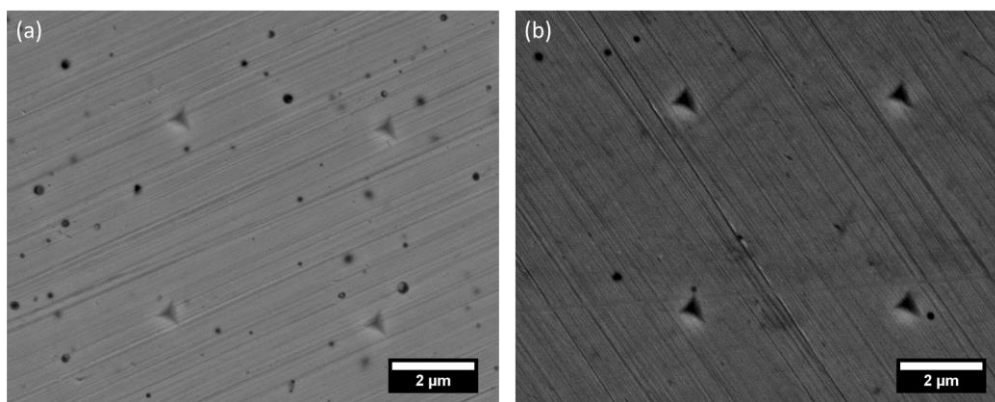
Figure 4.10: Representative SEM images of 1 mN max load indents performed on (a) ST-BM and (b) ST-GA.

4.2.2.1   5 mN Max Load

The nanoindentation hardness values of the single tracks with a max load of 5 mN are shown in Figure 4.11. The hardness of ST-BM-360-40, ST-BM-410-40, and ST-BM-460-40 was found to be 4.6 GPa, 4.6 GPa, and 4.5 GPa, respectively. The hardness of ST-GA-360-40, ST-GA-410-40, and ST-GA-460-40 was found to be 3.8 GPa, 3.7 GPa, and 3.9 GPa, respectively. This corresponds to an average hardness in ST-GA and ST-BM of 3.8 GPa and 4.6 GPa, respectively.
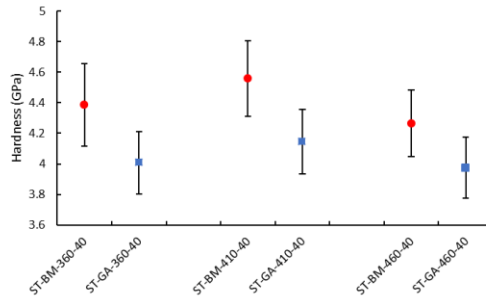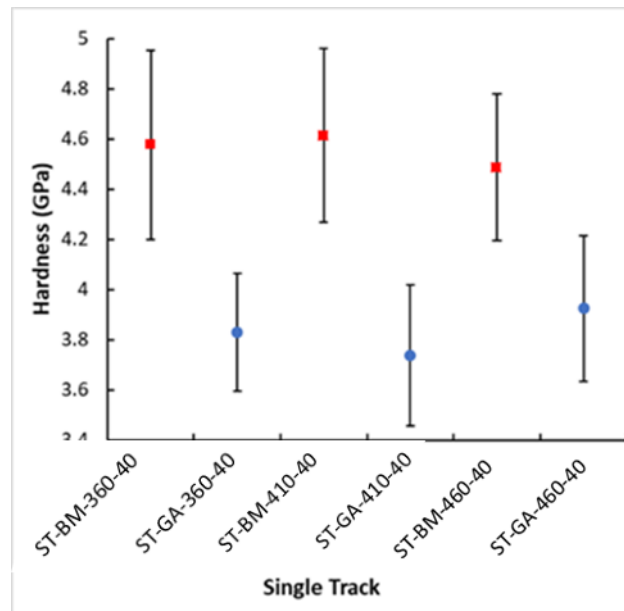

Figure 4.11: Nanoindentation hardness of (red) ST-BM and (blue) ST-GA at 5 mN max load.

SEM images of indents performed on ST-GA and ST-BM with a 5 mN max load show that pores are smaller than plastic deformation of indents (Figure 4.12). While porosity is still expected to decrease the accuracy of the hardness measurements, the increased interaction volume of the indents with a higher max load better represent the material properties of the single tracks as the plastic deformation zone of the indents is larger than the pores. The ST-BM were found to be 21% harder than ST-GA. The local hardness values

show fluctuations when the x-position and y-position are varied in the single tracks, as shown in Figure 4.13 and Figure 4.14. However, the change in the local hardness values does not show a trend of the dependency of hardness on position.
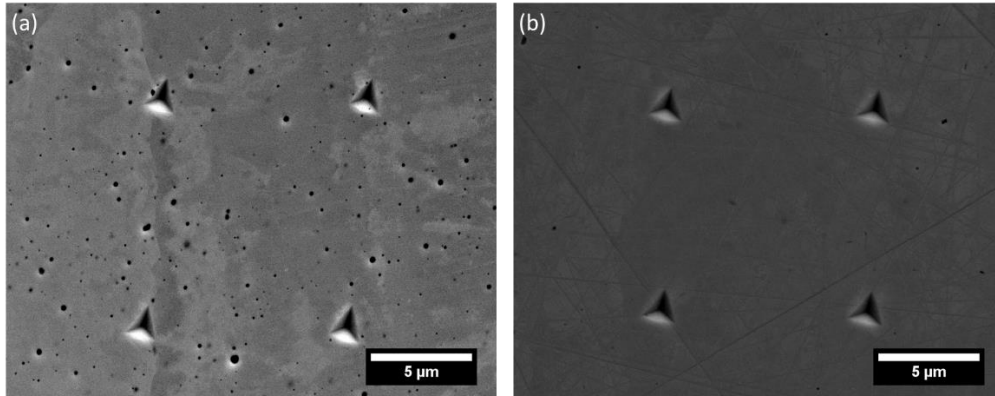
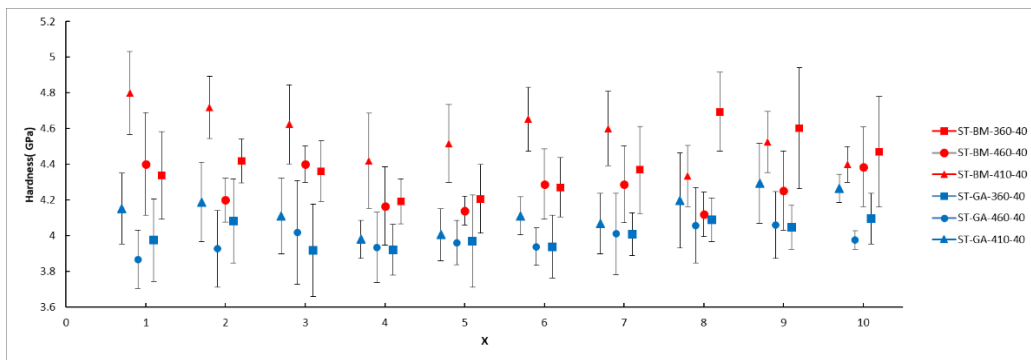**Figure 4.12: Representative SEM images of 5 mN max load indents performed on (a) ST-BM and (b) ST-GA.**
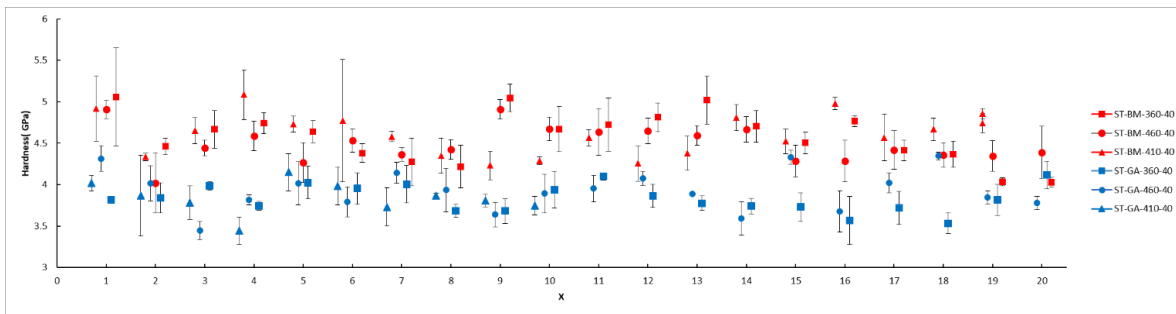
Figure 4.13: Dependence of nanoindentation hardness on x position of (red) ST-BM and (blue) ST-GA at 5 mN max load.

Figure 4.14: Dependence of nanoindentation hardness on y position of (red) ST-BM and (blue) ST-GA at 5 mN max load.

Chapter 5   Conclusions and vision of Future Work

Significant resource consumption, e.g., energy and inert gas, are required to produce GA powders to be used as feedstock in metal AM, leading to high costs and limited availability in alloy compositions. To fulfill the growing demand of sustainable feedstock production for metal AM, the present work proposed an alternati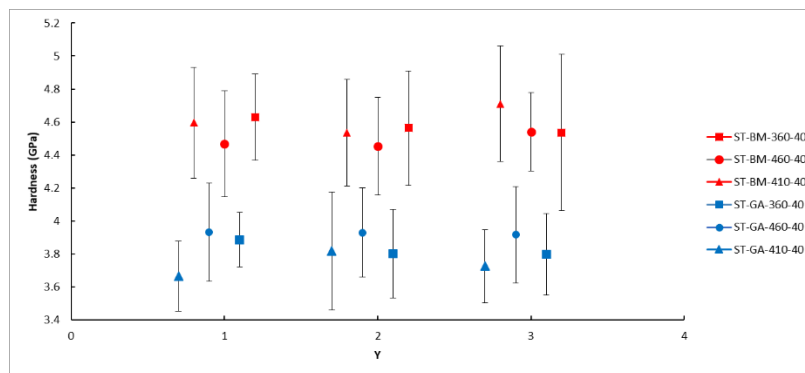ve powder production method based on recycling of metal machining waste via planetary ball milling. Increases in particle size reduction rate and spherical morphology formation were realized through theoretical analysis and experimental investigation. The ball milled powders created from machining waste were successfully used as feedstock in an AM technique called LENS® to deposit single tracks, using processing parameters common for GA powder of a similar composition. This chapter will summarize the key findings in this work. Vision of future work in this field is also outlined.

5.1   Ball Milling of Waste Chips to Produce Powder

The theoretical analysis of the force per impact and the maximum deformation depth in a powder particle suggest that ball diameter is a primary factor that determines the particle size reduction and morphology evolution during ball milling. With a consistent ball-to-powder weight ratio, when the ball diameter is increased to two times that of the previous one (e.g., from 6 mm to 12 mm), the impact frequency is decreased to 1/8 that of the previous value, while the force per impact is increased to eight times that of the previous value. In addition, each impact results in an increase in the maximum deformation depth to three times that of the previous value. Although the theoretical model has limitations due to only accounting for direct impacts and assuming all forces are transferred into one given particle,

it provides fundamental insight into the role of ball diameter in the plastic deformation in a powder particle during ball milling.

Particle size refinement and morphology evolution of the powders observed in the experimental work agree well with the theoretical analysis. Φ-20 balls effectively break down the 5-20 mm machining chips into particles with a size of several hundred microns within 24 hours. Continued milling with Φ-6 balls increases the frequency of low-force impacts and eventually reduces the powder particle size to a range of 38-150 μm, with a near spherical morphology. A phase change from metastable austenite to martensite, observed by XRD, may contribute to a decrease in the maximum deformation depth by increasing the yield strength of the material. It was also found that ball milling in ethanol had a negative effect on the final morphology. These powders were found to be flattened and flakey.

To expand the application of ball milling to convert machining waste to useful powders, continued research is in demand to investigate the effect of initial feedstock material properties on the final characteristics of the powder products when different ball milling parameters are used. Machining waste from some metals and alloys that are commonly of high costs, such as titanium (Ti) or aluminum (Al) alloys, worth to be recycled to produce powder that can be used in AM or other powder metallurgical techniques. In the manufacturing process of bulk titanium, granules of crushed titanium sponge are formed, and they could be utilized as well as machining waste to form powder by ball milling [108]. This would eliminate the need to press and re-melt titanium alloys to produce powder or other bulk titanium. Both Al and Ti are of interest in metal AM due to their structural properties. Rapid oxidation of the Al and Ti alloys and possible ignition make ball milling at

room temperature a challenge. Cryomilling may be an alternative ball milling strategy to be considered.

5.2   Characterization of the Powders

The powders fabricated from stainless steel machining chips via ball milling were characterized in terms of particle size, morphology, composition, and hardness. The characteristics of the ball milled powders were compared to those of GA powder that is commonly used as feedstock in metal AM. Several particle size ranges and powder morphologies have been used in different metal AM consolidation techniques, but it is generally accepted that powder with a more spherical morphology and a narrow particle size distribution will produce the best results in metal AM [2,10,11,26,28,30,69,79].

In this work, 69 wt.% of powder has a particle size in the range (38-150 μm) ideal for LENS® deposition after 60 hours of milling when the dual-stage ball milling approach was used. In contrast, less than 4 wt.% of powder was within this same particle size range after 60 hours when either single-stage milling approach was applied. It was found that milling with balls of large size was more effective in breaking down the initial machining chips to particles with sizes of several hundred microns within 24 hours, while milling with balls of small size were more effective in reducing this intermediate particle size to 38-150 μm.

Phase identification via XRD showed that the primary austenitic phase in 304L machining chips transformed to a primary martensitic phase after ball milling. This phase transformation is induced by the plastic deformation resulting from the repeated impacts on the powder from the ball-powder-ball collisions. The formation of martensite contributes to increased hardness and decreases in maximum deformation depth in the powder during ball milling.

The hardness, as determined by nanoindentation, of the ball milled powder was 57% higher than the hardness of the GA powder. The higher hardness of the ball milled powder resulted from increased dislocation density, reduced grain size, and the increased fraction of martensite. Characterization of grain size and dislocation density needs to be performed using transmission electron microscopy (TEM). It is significant to investigate how strengthening that occurs during ball milling affects the maximum deformation depth in the powder and subsequently changes the morphology evolution. Future work is needed to incorporate the simultaneous change in the mechanical properties of the chips or powders during ball milling into the models that predict the deformation depth. This work would help to identify milling parameters that efficiently form powder suitable for metal AM.

BM-2Stg-60hr powder showed near-spherical morphology with an average aspect ratio of approximately 1.37. It was observed that the morphology of the powders changed from flattened to near-spherical by the increase in milling time in the second stage where Φ-20 balls were replaced by Φ-6 balls. The change in morphology of the powder may be attributed to both the increased resistance to plastic deformation of the powder and the lower maximum deformation depth induced by small balls. The increased resistance to plastic deformation as chips turn to powder was quantified by a 44% increase in nanoindentation hardness. The maximum deformation depth of powder impacted by Φ-6 balls was found to be 85% lower than the maximum deformation depth of powder impacted by Φ-20 balls. In addition, the frequency of impacts is 37 times higher when milling with Φ-6 balls vs. Φ-20 balls. Consequently, a near-spherical morphology is achieved by the increased frequency of low-force impacts from the Φ-6 balls.

Another characteristic of the powders that is important for metal AM is flowability. In metal AM, powder with high flowability moves through equipment efficiently while powder with low flowability may get trapped. Powder flowability is not directly measured by a single test, but is found by the characterization of multiple material properties [109]. Common techniques used to determine properties that affect powder flowability include gravity assisted methods such as Hall and Carney funnel testing, angle of repose, and avalanche angle. Hall and Carney funnel testing is performed by measuring how long it takes for a certain mass of powder to exit the bottom of a funnel [2,8]. The difference between Hall funnel testing and Carney funnel testing is the diameter of the opening. Angle of repose is tested by slowly adding powder to a point in the center of a circular disk with a known cross section. The height is then measured and a simple trigonometry relationship is used to determine the critical angle at which the powder flows [2,8,18]. Sufficient powder must be used for angle of repose testing such that powder overflows off the edge of the disk. Avalanche angle is measured by rotating powder in a slow turning cylinder turned on edge (similar to how a roller mill operates) and measuring the average angle that the powder falls [19]. Shear cell testing can also be performed by the rotation of oppositely turning circular plates with powder between them to measure powder-powder friction and powder-wall friction [20–23]. However, each of these flowability testing methods is not indicative of forced powder flow by inert gas. Therefore, further flowability characterization methods need to be developed to better represent the flow of powder through powder-feed metal AM equipment such as LENS®.

5.3 Metal Additive Manufacturing

Ball milled powder was successfully deposited into single tracks via LENS®. Characterization of the deposited single tracks indicate continuity, adequate penetration into the substrate, and uniformity in melt pool geometry. Minimal differences in grain morphology, orientation, and phase are observed between single tracks made from BM-2Stg-60hr powder and the single tracks created from GA powder using identical LENS® deposition parameters. Homogeneity in chemical composition and porosity less than 4 vol.% was observed in both types of single tracks. However, EDS of the cross section of single tracks suggest the average Ni content in ST-GA (9.7 wt.%) is higher than that in ST-BM (8.0 wt.%).

Nanoindentation hardness values of the single tracks were measured to investigate the mechanical properties of ST-BM and ST-GA. ST-BM exhibited a higher hardness than ST-GA, which was attributed to the difference in Ni content. While the Ni content of both ST-BM and ST-GA are within the ranges suitable for a 304L alloy (8-12 wt.% Ni), the higher content of Ni in the ST-GA may contribute to a higher volume fraction of austenite, as Ni is used to stabilize austenite at room temperature. As a result, the martensite content in ST-BM is higher than that in ST-GA, which contributes to the higher hardness of the ST-BM.

While deposition of single tracks verified the feasibility of using ball milled powder in metal AM, future work to deposit larger build (>100 layers) using the ball milled powder is proposed to provide a thorough understanding of how the characteristics of feedstock powder affect the bulk properties of the final parts. Large build volumes allow for the testing of bulk mechanical properties such as yield strength and ultimate tensile strength. Intermediate build volumes (~3-4 layers) is also useful to determine the re-melting characteristics of previous build layers.

Powder fabricated by ball milling of other complex material systems such as Al and Ti alloys should also be tested using each of the above methods to investigate potential differences in the properties of the final parts obtained by metal AM when alternative feedstock is used. Melt pool geometry and deposition energy density may need to be optimized for different material systems due to differences in melting and re-solidification rate, thermal conductivity, and absorption of laser energy. Despite that significant future work is in demand to continue to bring an advance in this field, this work successfully demonstrated it is feasible to use ball milled stainless steel powder created from machining chips as an alternative feedstock in metal AM, which will benefit the sustainability of this advanced manufacturing process.

References

[1]   S. Ford, M. Despeisse, J. Clean. Prod. 137 (2016) 1573–1587.
[2]   J.H. Tan, W.L.E. Wong, K.W. Dalgarno, Addit. Manuf. 18 (2017) 228–255.
[3]   S.H. Huang, P. Liu, A. Mokasdar, L. Hou, Int. J. Adv. Manuf. Technol. 67 (2013) 1191–1203.
[4]   N. Serres, D. Tidu, S. Sankare, F. Hlawka, J. Clean. Prod. 19 (2011) 1117–1124.
[5]   F.L. Bourhis, O. Kerbrat, J.-Y. Hascoet, P. Mognol, Int. J. Adv. Manuf. Technol. 69 (2013) 1927–1939.
[6]   W.E. Frazier, J. Mater. Eng. Perform. 23 (2014) 1917–1928.
[7]   K. Ma, T. Smith, E.J. Lavernia, J.M. Schoenung, Procedia Manuf. 7 (2017) 198–204.
[8]   I.E. Anderson, E.M.H. White, R. Dehoff, Curr. Opin. Solid State Mater. Sci. (n.d.).
[9]   H. Zhang, C.H. Zhang, Q. Wang, C.L. Wu, S. Zhang, J. Chen, A.O. Abdullah, Opt. Laser Technol. 101 (2018) 363–371.
[10]   S. Hoeges, A. Zwiren, C. Schade, Met. Powder Rep. 72 (2017) 111–117.
[11]   R. Li, Y. Shi, Z. Wang, L. Wang, J. Liu, W. Jiang, Appl. Surf. Sci. 256 (2010) 4350–4356.
[12]   K. Mahmood, W.U.H. Syed, A.J. Pinkerton, Opt. Lasers Eng. 49 (2011) 240–247.
[13]   K. Mahmood, A.J. Pinkerton, Proc. Inst. Mech. Eng. Part B J. Eng. Manuf. 227 (2013) 520–531.
[14]   K. Mahmood, N. Stevens, A.J. Pinkerton, J. Mater. Process. Technol. 212 (2012) 1271–1280.
[15]   A. Popovich, V. Sufiiarov, (2016).
[16]   S.M. Yusuf, N. Gao, Mater. Sci. Technol. 33 (2017) 1269–1289.
[17]   V. Ganesan, K.A. Rosentrater, K. Muthukumarappan, Biosyst. Eng. 101 (2008) 425–435.
[18]   D. Geldart, E.C. Abdullah, A. Hassanpour, L.C. Nwoke, I. Wouters, China Particuology 4 (2006) 104–107.
[19]   A.B. Spierings, M. Voegtlin, T. Bauer, K. Wegener, Prog. Addit. Manuf. 1 (2016) 9–20.
[20]   S.V. Søgaard, T. Pedersen, M. Allesø, J. Garnaes, J. Rantanen, Int. J. Pharm. 475 (2014) 315–323.
[21]   S. Koynov, B. Glasser, F. Muzzio, Powder Technol. 283 (2015) 103–112.
[22]   U. Zafar, C. Hare, G. Calvert, M. Ghadiri, R. Girimonte, B. Formisani, M.A.S. Quintanilla, J.M. Valverde, Powder Technol. 286 (2015) 807–816.
[23]   P.D. Jager, T. Bramante, P.E. Luner, J. Pharm. Sci. 104 (2015) 3804–3813.
[24]   M.K. Stanford, D. Eylon, C. DellaCorte, J. Therm. Spray Technol. 13 (2004) 586–592.
[25]   R.P. Zou, A.B. Yu, Powder Technol. 88 (1996) 71–79.
[26]   J.A. Slotwinski, E.J. Garboczi, P.E. Stutzman, C.F. Ferraris, S.S. Watson, M.A. Peltz, J. Res. Natl. Inst. Stand. Technol. 119 (2014) 460.
[27]   ResearchGate (n.d.).
[28]   L.C. Ardila, F. Garciandia, J.B. González-Díaz, P. Álvarez, A. Echeverria, M.M. Petite, R. Deffley, J. Ochoa, Phys. Procedia 56 (2014) 99–107.
[29]   U. Scipioni Bertoli, G. Guss, S. Wu, M.J. Matthews, J.M. Schoenung, Mater. Des. 135 (2017) 385–396.

[30] H. Irrinki, M. Dexter, B. Barmore, R. Enneti, S. Pasebani, S. Badwe, J. Stitzel, R. Malhotra, S.V. Atre, JOM 68 (2016) 860–868.

[31] S. Dietrich, M. Wunderer, A. Huissel, M.F. Zaeh, Procedia Manuf. 6 (2016) 88–95.

[32] E.J. Lavernia, N.J. Grant, Mater. Sci. Eng. 98 (1988) 381–394.

[33] K. Ma, H. Wen, T. Hu, T.D. Topping, D. Isheim, D.N. Seidman, E.J. Lavernia, J.M. Schoenung, Acta Mater. 62 (2014) 141–155.

[34] T.B. Holland, U. Anselmi-Tamburini, A.K. Mukherjee, Scr. Mater. 69 (2013) 117–121.

[35] X.J. Liu, Z.Z. Xu, H. Xiao, D.K. Park, K.W. Kim, Y.C. Kim, S.H. Yeon, I.S. Ahn, Powder Technol. 259 (2014) 117–124.

[36] R. Shashanka, D. Chaira, Powder Technol. 278 (2015) 35–45.

[37] E. Afshari, M. Ghambari, Mater. Des. 103 (2016) 201–208.

[38] C.E. da Costa, W.C. Zapata, M.L. Parucker, J. Mater. Process. Technol. 143–144 (2003) 138–143.

[39] M.H. Enayati, M.R. Bafandeh, S. Nosohian, J. Mater. Sci. 42 (2007) 2844–2848.

[40] D.B. Witkin, E.J. Lavernia, Prog. Mater. Sci. 51 (2006) 1–60.

[41] L. Kurmanaeva, T.D. Topping, H. Wen, H. Sugahara, H. Yang, D. Zhang, J.M. Schoenung, E.J. Lavernia, J. Alloys Compd. 632 (2015) 591–603.

[42] C. Suryanarayana, Prog. Mater. Sci. 46 (2001) 1–184.

[43] Y. Xun, F.A. Mohamed, E.J. Lavernia, Metall. Mater. Trans. A 35 (2004) 573–581.

[44] E. Hall, Yield Point Phenomena in Metals and Alloys, Springer Science & Business Media, 2012.

[45] Y.X. Liang, Z.M. Wu, E.G. Fu, J.L. Du, P.P. Wang, Y.B. Zhao, Y.H. Qiu, Z.Y. Hu, Int. J. Refract. Met. Hard Mater. 67 (2017) 1–8.

[46] S. Jun, D. Zengjie, L. Zhonghua, T. Mingjing, Int. J. Fract. 42 (1990) R39–R42.

[47] M. Magini, A. Iasonna, Mater. Trans. JIM 36 (1995) 123–133.

[48] J.B. Fogagnolo, F. Velasco, M.H. Robert, J.M. Torralba, Mater. Sci. Eng. A 342 (2003) 131–143.

[49] C.C. Doumanidis, H.A. Al Kaabi, A.S.M. Alzaabi, I.E. Gunduz, C. Rebholz, C.C. Doumanidis, Powder Technol. 301 (2016) 1077–1084.

[50] A.I. Gusev, A.S. Kurlov, Nanotechnology 19 (2008) 265302.

[51] P.P. Chattopadhyay, I. Manna, S. Talapatra, S.K. Pabi, Mater. Chem. Phys. 68 (2001) 85–94.

[52] M. Abdellahi, M. Bhmanpour, M. Bahmanpour, Ceram. Int. 40 (2014) 16259–16272.

[53] A. Canakci, T. Varol, J. Clean. Prod. 99 (2015) 312–319.

[54] X. Yao, Y.F. Zheng, J.M. Liang, D.L. Zhang, Mater. Sci. Eng. A 648 (2015) 225–234.

[55] M.P. Dallimore, P.G. McCormick, Mater. Trans. JIM 37 (1996) 1091–1098.

[56] P. Le Brun, L. Froyen, L. Delaey, Mater. Sci. Eng. A 161 (1993) 75–82.

[57] H. Mio, J. Kano, F. Saito, Chem. Eng. Sci. 59 (2004) 5909–5916.

[58] P.J. Desré, Nanostructured Mater. 8 (1997) 687–701.

[59] J. Trapp, B. Kieback, Acta Mater. 61 (2013) 310–320.

[60] J. Johnson, B.K. Reck, T. Wang, T.E. Graedel, Energy Policy 36 (2008) 181–192.

[61] S. Nakamura, Y. Kondo, K. Nakajima, H. Ohno, S. Pauliuk, Environ. Sci. Technol. 51 (2017) 9469–9476.

[62] J. Gronostajski, H. Marciniak, A. Matuszak, J. Mater. Process. Technol. 106 (2000) 34–39.

[63] J.M. Liang, M.T. Jia, X.Q. Guo, D.L. Zhang, Mater. Sci. Eng. A 590 (2014) 307–313.

[64] T. Zhang, Z. Ji, S. Wu, Mater. Des. 32 (2011) 2742–2748.

[65] R. Chiba, T. Nakamura, M. Kuroda, J. Mater. Process. Technol. 211 (2011) 1878–1887.

[66] L.A. Jacobson, J. McKittrick, Mater. Sci. Eng. R Rep. 11 (1994) 355–408.

[67] M.W. Chase, J. Phys. Chem. Ref. Data, Monograph 9 (1998) 1–1951.

[68] T. DebRoy, H.L. Wei, J.S. Zuback, T. Mukherjee, J.W. Elmer, J.O. Milewski, A.M. Beese, A. Wilson-Heid, A. De, W. Zhang, Prog. Mater. Sci. 92 (2018) 112–224.

[69] D. Herzog, V. Seyda, E. Wycisk, C. Emmelmann, Acta Mater. 117 (2016) 371–392.

[70] E. Gaffet, G. Le Caër, in: C. Bréchignac, P. Houdy, M. Lahmani (Eds.), Nanomater. Nanochemistry, Springer Berlin Heidelberg, Berlin, Heidelberg, 2007, pp. 455–471.

[71] C.C. Koch, J.D. Whittenberger, Intermetallics 4 (1996) 339–355.

[72] F.J. Gotor, M. Achimovicova, C. Real, P. Balaz, Powder Technol. 233 (2013) 1–7.

[73] S.S. Dheda, C. Melnyk, F.A. Mohamed, Mater. Sci. Eng. A 584 (2013) 88–96.

[74] M.A. Atwater, D. Roy, K.A. Darling, B.G. Butler, R.O. Scattergood, C.C. Koch, Mater. Sci. Eng. A 558 (2012) 226–233.

[75] B.K. VanLeeuwen, K.A. Darling, C.C. Koch, R.O. Scattergood, Mater. Sci. Eng. A 528 (2011) 2192–2195.

[76] J. Esquivel, K.A. Darling, H.A. Murdoch, R.K. Gupta, Metall. Mater. Trans. A (2018).

[77] B. Ahn, A.P. Newbery, E.J. Lavernia, S.R. Nutt, Mater. Sci. Eng. A 463 (2007) 61–66.

[78] N. Yang, J.K. Yee, Z. Zhang, L. Kurmanaeva, P. Cappillino, V. Stavila, E.J. Lavernia, C. San Marchi, Acta Mater. 82 (2015) 41–50.

[79] H.P. Tang, M. Qian, N. Liu, X.Z. Zhang, G.Y. Yang, J. Wang, JOM 67 (2015) 555–563.

[80] M.H. Enayati, M.R. Bafandeh, J. Alloys Compd. 454 (2008) 228–232.

[81] P. Mallick, N.K. Tewary, S.K. Ghosh, P.P. Chattopadhyay, Mater. Charact. 133 (2017) 77–86.

[82] A.M. Beese, D. Mohr, Acta Mater. 59 (2011) 2589–2600.

[83] J. Man, M. Smaga, I. Kuběna, D. Eifler, J. Polák, Eng. Fract. Mech. (n.d.).

[84] Z. Wu, Y. Huang, Procedia Eng. 99 (2015) 1323–1329.

[85] W. Zeng, H. Yuan, Mater. Sci. Eng. A 679 (2017) 249–257.

[86] I. Yadroitsev, A. Gusarov, I. Yadroitsava, I. Smurov, J. Mater. Process. Technol. 210 (2010) 1624–1631.

[87] M. Sadowski, L. Ladani, W. Brindley, J. Romano, Addit. Manuf. 11 (2016) 60–70.

[88] H. Gong, H. Gu, K. Zeng, J.J.S. Dilip, D. Pal, B. Stucker, D. Christiansen, J. Beuth, J.J. Lewandowski, in: Solid Free. Fabr. Symp., 2014, pp. 256–267.

[89] Y. Yang, D. Gu, D. Dai, C. Ma, Mater. Des. 143 (2018) 12–19.

[90] W.E. King, H.D. Barth, V.M. Castillo, G.F. Gallegos, J.W. Gibbs, D.E. Hahn, C. Kamath, A.M. Rubenchik, J. Mater. Process. Technol. 214 (2014) 2915–2925.

[91] R. Trivedi, S.A. David, M.A. Eshelman, J.M. Vitek, S.S. Babu, T. Hong, T. DebRoy, J. Appl. Phys. 93 (2003) 4885–4895.

[92] A.J. Wilkinson, T.B. Britton, Mater. Today 15 (2012) 366–376.

[93] X. Wang, K. Chou, JOM 69 (2017) 402–408.

[94] A. Keshavarzkermani, M. Sadowski, L. Ladani, J. Alloys Compd. 736 (2018) 297–305.

[95] Q. Jia, D. Gu, J. Alloys Compd. 585 (2014) 713–721.

[96] W.C. Oliver, G.M. Pharr, J. Mater. Res. 7 (1992) 1564–1583.

[97] G.M. Pharr, W.C. Oliver, F.R. Brotzen, J. Mater. Res. 7 (1992) 613–617.

[98] C.E. da Costa, W.C. Zapata, M.L. Parucker, J. Mater. Process. Technol. 143 (2003) 138–143.

[99]   H. Hertz, D.E. Jones, G.A. Schott, Miscellaneous Papers, London: Macmillan, New York, Macmillan and co., 1896.

[100] S.D. Washko, G. Aggen, Wrought Stainless Steels, Properties and Selection: Irons, Steels, and High-Performance Alloys, ASM International, 1990.

[101] A. Wolfenden, K. Suzuki, J. Fukakura, H. Kashiwaya, J. Test. Eval. 16 (1988) 190.

[102] A. Hedayati, A. Najafizadeh, A. Kermanpur, F. Forouzan, The Effect of Cold Rolling Regime on Microstructure and Mechanical Properties of AISI 304L Stainless Steel, 2010.

[103] J.W. Elmer, S.M. Allen, T.W. Eagar, Microstructural Development during Solidification of Stainless Steel Alloys, 1988.

[104] L. Ladani, Metall. Mater. Trans. A 46 (2015) 3835–3841.

[105] H. Inoue, T. Koseki, Nippon Steel Tech. Rep. 95 (2007) 62–70.

[106] I.I. Musabirov, R.R. Mulyukov, V.V. Koledov, IOP Conf. Ser. Mater. Sci. Eng. 82 (2015) 012064.

[107] S.M. Collins, P.A. Midgley, Ultramicroscopy 180 (2017) 133–141.

[108] B. Dutta, F.H. (Sam) Froes, Met. Powder Rep. 72 (2017) 96–106.

[109] A. Santomaso, P. Lazzaro, P. Canu, Chem. Eng. Sci. 58 (2003) 2857–2874.